Materials Advances

ROYAL SOCIETY OF CHEMISTRY

PAPER

View Article Online
View Journal | View Issue

Cite this: *Mater. Adv.*, 2025, 6, 5971

Localized photothermal–chemotherapy synergy *via* Bi_2S_3 and sorafenib co-loaded dissolvable microneedles: a non-invasive precision delivery approach for melanoma suppression†

Mahsa Akbari,[a] Maryam Toolabi,[a] Atefeh Malek-Khatabi,[c] Mohammad Reza Eskandari,[d] Bo Zhi Chen,[ef] Xin Dong Guo[ef] and Mohammad-Ali Shahbazi*[b]

Skin cancer, particularly melanoma, is currently treated through various approaches, including surgery, radiotherapy, and chemotherapy. However, these methods have significant limitations and cause severe side effects. This underscores the pressing need for more effective therapies. Given that this disease appears on the skin surface, it is imperative to have a therapeutic system for topical drug delivery while minimizing systemic distribution. Microneedling is a novel transdermal drug delivery system that creates micropores on the skin surface to bypass the stratum corneum and achieve successful drug delivery to the skin sublayers, in a non-invasive manner. In this study, a dissolvable microneedle (MN) patch is created using polyvinylpyrrolidone (PVP), a water-soluble, biocompatible, and biodegradable polymer. Bismuth sulfide (Bi_2S_3) nanoparticles (NPs), as a photothermal therapy (PTT) agent, and sorafenib (SFN) for chemotherapy against cancer are co-encapsulated within the MN patch. The Bi_2S_3-SFN-loaded MN arrays exhibit strong mechanical properties for skin insertion, enabling them to penetrate tumors, dissolve, and release their therapeutic cargos directly within the tumor tissue. Upon exposure to an NIR laser, Bi_2S_3 NPs exhibit a photothermal effect, effectively inhibiting cancer cell proliferation. When combined with the chemotherapeutic capability of SFN, this approach shows great promise in achieving complete tumor suppression. In addition, the local administration of the MNs results in high biosafety and biocompatibility toward healthy tissues *in vivo*.

Received 10th June 2025,
Accepted 11th July 2025

DOI: 10.1039/d5ma00623f

rsc.li/materials-advances

1. Introduction

Melanoma is an aggressive and deadly form of skin cancer with a rising incidence worldwide.[1,2] The selection of an appropriate treatment method for melanoma is influenced by various factors, including the cancer's stage, primary melanoma thickness, rate of melanoma growth, and site of melanoma proliferation. Surgical intervention, particularly for localized melanoma, is the predominant treatment modality. Nevertheless, in the case of unresectable tumors, surgery is not a viable option. Moreover, for patients with advanced melanoma (up to stage II), surgery has a limited curative response and necessitates adjuvant therapy.[3] Besides the long recovery period, surgical management for melanoma is limited by poor patient compliance, high risk of infection, scarring, and nerve damage.[4] Immunotherapy,[5] targeted therapy,[6,7] radiotherapy,[8] and chemotherapy[9] are the other most common treatment strategies for melanoma. However, they come with certain limitations and adverse effects. Immunotherapy can disrupt immune tolerance, potentially leading to immune-related disorders such as dermatological, gastrointestinal, and endocrine abnormalities. In addition, the high cost and poor bioavailability of these therapies are major concerns that warrant attention.[10]

Radiation therapy is a feasible treatment for melanoma that induces reactive oxygen species (ROS) primarily through water

[a] Department of Pharmaceutical Nanotechnology, School of Pharmacy, Zanjan University of Medical Sciences, 45139-56184 Zanjan, Iran
[b] Department of Biomaterials and Biomedical Technology, The Personalized Medicine Research Institute (PRECISION), University Medical Center Groningen (UMCG), University of Groningen, Antonius Deusinglaan 1, 9713 AV, Groningen, The Netherlands. E-mail: m.a.shahbazi@umcg.nl
[c] Department of Pharmaceutical Biomaterials, Faculty of Pharmacy, Tehran University of Medical Sciences, Tehran, 1417614411, Iran
[d] Department of Pharmacology and Toxicology, School of Pharmacy, Zanjan University of Medical Science, 45139-56184 Zanjan, Iran
[e] State Key Laboratory of Organic–Inorganic Composites, Beijing University of Chemical Technology, Beijing 100029, China
[f] Beijing Laboratory of Biomedical Materials, College of Materials Science and Engineering, Beijing University of Chemical Technology, Beijing 100029, China

† Electronic supplementary information (ESI) available. See DOI: https://doi.org/10.1039/d5ma00623f

radiolysis triggered by ionizing radiation. These ROS contribute to cellular damage and tumor cell death. However, the hypoxic nature of tumors reduces the availability of molecular oxygen, which is essential for stabilizing ROS and maximizing radiation therapy efficacy. While high-dose radiation therapy is proposed as a solution, it can cause systemic side effects such as bone marrow suppression and infertility.[11] Alternatively, PTT, as a radiotherapy approach that converts near-infrared (NIR) light to heat, can be a better alternative local therapy for local melanoma cancer therapy.[12,13] Hyperthermia can induce cancer cell apoptosis due to tumor tissue's low thermal tolerance compared to normal tissue.[14,15] Bismuth-based nanostructures have emerged as promising agents for PTT because of low toxicity, high yield in X-ray and NIR absorption, high atomic number, and abundance, which have a significant impact on the manufacturing cost.[16–18] Recent studies have demonstrated that relying solely on PTT for cancer treatment is insufficient to achieve complete tumor eradication. This is because NIR light is absorbed and scattered, reducing its ability to penetrate deep into tumor tissues.[19] Therefore, combining PTT with other cancer treatment strategies is recommended. Chemotherapy is the most widely used systemic treatment for melanoma that can inhibit the growth of cancer cells and eliminate them. However, it has several disadvantages, such as reduced quality of life, DNA damage in normal tissue, acceleration of aging, and the multidrug resistance effect.[20,21] Considering these limitations, combining low-dose chemotherapy with other therapies can reduce side effects while enhancing the therapeutic efficacy through synergistic effects.[22,23] However, key challenges that would persist are improving drug localization in the disease site, reducing systemic toxicity, and establishing a painless and noninvasive medical intervention. To do so, local drug delivery systems are designed to overcome physiological barriers and effectively target drugs directly to the site of action using minimum therapeutic doses.

MNs are an emergent platform to improve drug diffusion and penetration into the skin. The micron-sized needles of MN arrays, by micropore creation on the skin surface, facilitate the direct delivery of drugs to the sublayers of the skin. In addition, MN arrays mitigate the first-pass metabolism effect on drugs and enhance their bioavailability, while minimizing systemic toxicity.[24,25] The exceptional benefits of this platform include its non-invasiveness, ease of use, adjustable loading capacity, patient compliance, and safety, which make this platform suitable for delivering high molecular weight drugs (*e.g.*, peptides and proteins),[26] DNA/RNA,[27] vaccines,[28] vitamins,[29] and cosmeceuticals[30] in various diseases. Dissolvable MNs represent an innovative drug delivery system made from various water-soluble polymers, which dissolve upon insertion into the skin, releasing the drug.[31] PVP-based MN patches considering their water solubility, biocompatibility, mechanical strength, and FDA approval have been researched in several cancer treatment studies.[32,33] The present work involves the synthesis of Bi_2S_3 NPs followed by their embedding, together with SFN, into PVP dissolvable MN patches. This study aims to investigate the efficacy of combining Bi_2S_3 NPs with SFN in PVP dissolvable MN patches as a therapeutic option for superficial melanoma. Bi_2S_3 NPs have been demonstrated to be efficient photothermal agents, converting NIR light to heat, which has shown promising results in combating tumor growth.[34] On the other hand, SFN is a chemotherapy drug and an inhibitor of Raf-1 and B-Raf serine/threonine kinases, which help suppress angiogenesis and tumor growth.[35,36] The efficacy of SFN against melanoma cells alone is relatively low. Therefore, we propose its combination with PTT to achieve a synergistic anti-tumor effect.

2. Experimental sections

2.1. Synthesis of Bi_2S_3 NPs

Bi_2S_3 NPs were prepared by using the coprecipitation method. Briefly, 40 mg thioacetamide, as the sulfur source, (C_2H_5NS; >98%, Merck, Germany) was dissolved in 1 mL deionized water (DIW) under vigorous stirring at 50 °C, and the prepared solution was added to 14 mL ethanol 96% (v/v) containing 3 mL DIW. In the next step, 80 mg bismuth(III) nitrate pentahydrate ($Bi(NO_3)_3{\cdot}5H_2O$; 98%, SAMCHUN, South Korea) was dissolved in 2 mL DIW/glycerol 85% (1 : 1; v/v) under stirring conditions, and was added to the above solution under constant stirring (4 h at 50 °C). For harvesting the Bi_2S_3 NPs and removing residual solvents and free thioacetamide or $Bi(NO_3)_3{\cdot}5H_2O$, the solution was washed 3 times with DIW and once with ethanol, followed by centrifugation for 10 min at 14 000 rpm in each step. After that, the obtained NPs were collected and dispersed in ethanol 96% (v/v). The probe sonication method was utilized to enhance the homogenization of the NPs in solution. The concentration of Bi_2S_3 NPs was determined by drying the defined volume of the solution at 70 °C in an oven and measuring the weight of the obtained powder. Then it was expressed in units of mg μL^{-1}.

2.2. Characterization of Bi_2S_3 NPs

The morphology and size distribution of NPs were determined by transmission electron microscopy (TEM, EM 208S, Philips) and scanning electron microscopy (SEM, FEI, Quanta 200). The surface charge of the NPs was measured using a zeta potential instrument (VASCO, Cordouan Technologies). The formation of Bi_2S_3 NPs, structural studies, qualitative elemental analysis, thermal analysis, mean surface area, pore volume, and pore diameter were carried out *via* Fourier transform infrared spectroscopy (FTIR, Bruker, Spectral range: 400–4000 cm^{-1}, Spectral resolution: 2 cm^{-1}), X-ray diffraction (XRD, PW1730, Philips, Cu Kα radiation, λ = 1.5406 Å, 2θ range: 10°–80°, step size: 0.02°, scan rate: 2° min^{-1}), energy dispersive X-ray (EDX, TESCAN MIRA2, TESCAN, primary energy: 25 keV, take-off angle: 35°, real time: 56.7 s, live time: 56.1 s), thermogravimetric (TGA, Q600, TA, nitrogen atmosphere, heating rate: 10 °C min^{-1}, temperature range: 25–800 °C), and Brunauer–Emmett–Teller (BET, Belsorp mini II, Microtrac Bel Corp, nitrogen adsorption at 77 K, surface area by BET method, pore size by BJH method) analyses, respectively.

The crystallite size for the obtained NPs and SFN was calculated using Debye–Scherrer's formula:

$$D = \frac{K\lambda}{\beta \cos\theta} \quad (1)$$

where D is the average crystallite size in nm, K indicates the Scherrer constant, which is equal to 0.94, λ shows the wavelength of X-ray radiation (λ_{Cu} = 0.154 nm), β is the full width at half maximum intensity (FWHM), and θ presents the Bragg's angle.[37]

The specific surface area (SSA) was also calculated by plotting $P/[V(P_0 - P)]$ *versus* relative pressure (P/P_0), and determining the slope and intercept of the linear portion of the BET plot, where P is the equilibrium pressure of the adsorbate gas, P_0 is the saturation pressure, and V is the volume of gas adsorbed at standard temperature and pressure.

2.3. PVP-Bi_2S_3 and PVP-Bi_2S_3-SFN preparation

To prepare the PVP-Bi_2S_3 solution, a defined amount of PVP K90 (Sigma-Aldrich, United States) was dissolved in DIW under stirring to form a 20% (w/v) solution, and before adjusting the volume, 200 μg mL^{-1} of the Bi_2S_3 NPs was added and the solution sonicated (ultrasonic bath) for 15 min. For drug loading, to achieve a 4500 μg mL^{-1} concentration of SFN (Baran Chemical and Pharmaceutical, Iran) in the final solution, a calculated weight of it was dissolved in a minimal volume of ethanol 96% (v/v) and then added to the above solution to form PVP-Bi_2S_3-SFN. To remove bubbles in the prepared solutions, they were centrifuged for 20 min at 8500 rpm, at 5 °C, and kept at refrigerator temperature until further usage.

2.4. Fabrication of MN patches

The MNs were prepared using a solvent-casting method and with uniform PDMS (polydimethylsiloxane) molds (Micropoint Technologies Pte Ltd, Singapore). Each needle is arranged in a 10 × 10 array with 800 μm height and 200 μm × 200 μm base length. To fabricate MN patches, 400 μL of PVP 20% (w/v), the PVP-Bi_2S_3 (Bi_2S_3: 400 μg mL^{-1}) or PVP-Bi_2S_3-SFN (SFN: 4500 μg mL^{-1}) was poured into the mold in solution form, followed by centrifugation at 4500 rpm for 20 min to permit complete filling of the materials into micron-sized cavities. The sample was left to partially dry in a desiccator for 1 hour. Subsequently, PVP (17% w/v) solution was added into the tip-embedded PDMS mold and centrifuged (4500 rpm, 15 min) to form the backing layer and remove bubbles. This step was repeated once more after 3 h. Ultimately, the MN patch was carefully peeled off after a drying step of 24 h. The morphology of dissolvable MN patches was observed using an optical microscope (Olympus, using a 4× and 10× lens, Japan) and SEM (MIRA3TESCAN-XMU, LVSTD detector, Germany).

2.5. Drug loading and release tests

A typical procedure was followed to determine the appropriate SFN loading amount. Initially, the drug's calibration curve was created through a series of SFN dilutions, and the resulting amount was measured with UV-Vis spectroscopy at 265 nm (by absorbance scanning, SFN showed a maximum absorbance at 265 nm wavelength). Next, six MNs made from PVP-Bi_2S_3-SFN solution were dissolved in 5 mL DMSO (as a surfactant) and PBS (1 : 2) at pH 7.4 and 37 °C with gentle stirring. The absorbance of the solution was measured at 265 nm to calculate the drug amount using the obtained line equation from the calibration curve.

To observe the release rate of SFN-loaded MN *in vitro* and predict the *in vivo* release behavior of SFN, one MN patch was immersed in 5 mL of DMSO and PBS (1 : 2) at pH 7.4 and placed in an incubator shaker (80 rpm; 37 °C). At specific time intervals (0, 0.5, 1, 2, 3, 4, 5, 10, 20, 30, 60, 90, 120, 180, 240, 300, and 360 min), 2 mL of the release medium was collected and replaced with the same amount of fresh medium. The collected samples were then analyzed by UV-Vis spectroscopy at 265 nm and quantified based on the linear calibration curve. The experiment was repeated three times.

2.6. *In vitro* photothermal activity

To evaluate the PT behavior, the prepared solutions containing Bi_2S_3 (100, 200, 400 μg mL^{-1}), PVP-Bi_2S_3, and PVP-Bi_2S_3-SFN were irradiated under NIR light (808 nm) at three different power densities (0.5, 1, and 1.5 W cm^{-2}) for 10 min. During irradiation, the temperature was measured at one-minute intervals using an infrared thermal camera, and thermal images were recorded to monitor the PT effect. To assess the photothermal stability and conversion efficiency (η) of Bi_2S_3, the PVP-Bi_2S_3-SFN suspension (Bi_2S_3: 400 μg mL^{-1}) was irradiated with an 808 nm NIR laser at 1.5 W cm^{-2} for 10 min (On phase). Following irradiation, the laser was turned off, allowing the irradiated solution to cool back to room temperature (Off phase). This on/off cycle was repeated five times, with temperature measurements recorded every 60 s during heating and every 30 s during cooling. η was calculated according to the following eqn (2):

$$\eta = \frac{hA(T_{Max} - T_{Surr}) - Q_{Dis}}{I(1 - 10^{-A_\lambda})} \quad (2)$$

where h is the heat transfer coefficient, A is the surface area of the measured sample, T_{Max} (62 °C) and T_{Surr} (24.5 °C) are the maximum steady-state temperature and the ambient temperature, respectively, and the temperature change ($T_{Max} - T_{Surr}$) is 37.5 °C. Q_{Dis} represents the heat dissipated to the surroundings, I is the laser power (1.5 W cm^{-2}), and A_λ expresses the absorbance intensity of the sample at 808 nm (4.5). To calculate the value of hA, the following eqn (3) was used:

$$\tau_s = \frac{m_D C_D}{hA} \quad (3)$$

where m_D (0.77 g) and C_D (4.2 J g^{-1} $°C^{-1}$) are the mass and heat capacity of the solvent, respectively. The system time constant (τ_s) was determined using the following eqn (4) and (5):

$$t = \tau_s \ln(\theta) \quad (4)$$

$$\theta = \frac{T - T_{Surr}}{T_{Max} - T_{Surr}} \quad (5)$$

By plotting time against the negative logarithm of the driving force temperature (θ), τ_s was calculated to be 196.9 s, and thus the hA was determined to be 0.02 W $°C^{-1}$. The baseline energy, dissipated by the container and DIW (Q_{Dis}), was calculated using eqn (6):

$$Q_{Dis} = \frac{m_w \times c_w(T_{Max} - T_{Surr})}{\tau_s} \quad (6)$$

where m_w (0.05 mg) is the mass of DIW irradiated with an 808 nm laser (1.5 W cm^{-2}) for 10 min, c_w (4.2 J g^{-1} $°C^{-1}$) is the heat capacity of DIW, and (T_{max} − T_{Surr}) is the temperature change observed in DIW (11.6 °C). The corresponding τ_s for DIW was found to be 184.08 s, yielding a Q_{Dis} value of 0.013 mW. Substituting the obtained values of hA and Q_{Dis} into eqn (2), the photothermal conversion efficiency (η) of the PVP-Bi_2S_3-SFN solution under 808 nm laser irradiation was calculated to be 49%. All tests were performed in triplicate.

2.7. *In vivo* photothermal effect

To investigate the PT behavior of the synthesized NPs, the prepared MNs were inserted onto the dorsal skin of a hair-removed mouse using an applicator. Once the needles dissolved, the backing of the MN was removed, and the insertion site was exposed to 808 nm NIR irradiation at a power density of 1.5 W cm^{-2} for 10 min. Temperature changes were recorded and scanned using an infrared thermal camera.

2.8. Hemocompatibility evaluation

The biocompatibility of materials was studied using a standard hemolysis assay by measuring the absorbance of released hemoglobin after red blood cells (RBCs) lysis.[38] For this purpose, human fresh blood samples were diluted three times with PBS buffer (pH 7.4), and the suspensions were centrifuged (3000 rpm for 6 min at room temperature). After removing the supernatants, the precipitated RBCs were washed five times with fresh PBS solution (pH 7.4). Finally, the erythrocytes were resuspended in PBS (1 : 19) to achieve a hematocrit (Hct) of 5% (v/v). The Hct (0.2 mL) was then added to each sample (0.8 mL) to achieve final concentrations of 25, 50, 200, and 400 μg mL^{-1} for the testing of the NP and 50, 100, 200, and 400 μg mL^{-1} for the PVP, PVP-Bi_2S_3, and PVP-Bi_2S_3-SFN solutions. Next, the samples were incubated for 1, 4, 8, 24, and 48 h at 37 °C. Positive (100% hemolysis) and negative (0% hemolysis) controls were used for each time point to enable comparison. The positive control was created by incubating Hct with DIW, and the negative control was created by incubating Hct with PBS. After the incubation period, the resulting solutions were centrifuged (6000 rpm for 5 min), and the absorbance of supernatants (150 μL) was measured at 540 nm using a plate reader (Infinite M200, Austria). To ensure accuracy, each sample was conducted in triplicate, and the hemolysis rate was determined using the following calculation (7):

$$\text{Hemolysis } \% = \frac{A_{sample} - A_0}{A_{100} - A_0} \times 100 \quad (7)$$

where A_{sample}, A_0, and A_{100} are the absorbance of samples, negative and positive controls, respectively. The hemocompatibility assay was approved by the Ethics Committee of Zanjan University of Medical Sciences (approval number IR.ZUMS.REC.1400.438) and was conducted according to the approved protocol.

2.9. Mechanical and insertion properties of MNs

To assess the mechanical properties of blank and loaded MNs, a universal testing machine (SANTAM, STM-20) was utilized. Initially, the heights of the MNs were determined using an optical microscope (Olympus, 4× and 10× lens, Japan). A single MN patch was then secured onto a stainless base probe with double-sided tape, and an axial force was applied by a moving sensor probe against the base probe at a constant speed of 1 mm min^{-1} and a force ranging from 15 N to 73 N. This range was selected to evaluate the overall mechanical resistance of the MN patch, and the upper limit was defined based on the observed point at which visible bending or structural deformation of the MN tips occurred. The force applied represents the total load on the patch, rather than on individual needles, as commonly reported in the literature.[39] When the sensor made contact with the needle tips, compression force and displacement were recorded. The reduction in the height of the needles was calculated using eqn (8):

$$\text{Reduction height } \% = \frac{H_1 - H_2}{H_1} \times 100 \quad (8)$$

where H_1 represents the initial height of the needles and H_2 represents the height of the needles after compression force was applied.

To investigate the penetration behavior of MNs through the skin, a model membrane, Parafilm M® was used. Parafilm M® is a thermoplastic material composed of hydrocarbon wax and polyolefin. For the experiment, a single sheet of Parafilm M® was cut into eight 4 cm^2 squares (with an approximate thickness of 127 μm per layer). These squares were then stacked on top of each other to simulate skin layers. The dissolvable MNs were applied to the surface of the stacked film using thumb pressure for 30 s. After removing the patch, the layers of Parafilm were carefully unfolded, and the number of puncture sites in each layer was counted under an optical microscope. To estimate the penetration depth and effectiveness of the needles, the penetration efficiency was determined by calculating the number of needle penetrations (N_p) relative to the total number of needles in each patch (N_t). The penetration percentage was then computed using the following equation:

$$\text{Penetration } \% = \frac{N_p}{N_t} \times 100 \quad (9)$$

2.10. Skin penetration ability

The penetration ability of the fabricated MNs was confirmed by trypan blue (0.4% w/w, $C_{34}H_{28}N_6Na_4O_{14}S_4$, Merck, Germany) loaded patches on the cadaver skin of a rat. Insertion of MNs was performed using an applicator for 1 min, and the treated skin was imaged. The MN-treated skin was also stained with hematoxylin and eosin (H&E) to observe the microchannel formation.

2.11. MN dissolution in the skin

A study was performed to investigate the *in vivo* dissolution behavior and rate of MNs and to evaluate their dissolution

profile. Initially, the fur on the dorsal skin of anesthetized rats and mice was shaved to facilitate MN insertion. The animals were then assigned to two experimental groups. In the first group, MNs were inserted into the skin for 2, 5, 10, and 20 min, while in the second group, the treatment durations were extended to 2, 5, 10, 20, 30, and 40 min. After each time point, the MN patches were removed, and the morphology of the dissolved MNs was examined under optical microscopy and SEM to assess the dissolution process.

2.12. Payload release in the skin

Fluorescein isothiocyanate (FITC) was loaded in the MN patches as a drug model to visualize the transdermal drug delivery ability and drug distribution in the skin after the insertion of MNs by confocal laser scanning microscopy (CLSM). After insertion of the MNs into the shaved and anesthetized dorsal skin of a rat (20 min) the treated skin was fixed in a 10% solution of formaldehyde. The skin sections were then visualized under CLSM (every 100 μm depth for a total depth of 1500 μm) in varied time intervals of 1, 4, and 8 h.

2.13. *In vivo* biocompatibility of the MNs

We conducted an *in vivo* biocompatibility assessment on adult Wistar rats weighing 250 ± 30 g. The rats were randomly divided into four groups of five and anesthetized before shaving their dorsal skin. Three of the groups were treated with MN patches made of PVP, PVP-Bi_2S_3, and PVP-Bi_2S_3-SFN, while one group received no treatment as a control. The MNs were applied every other day for five days, and on the final day, blood samples were taken from animals for biochemical and hematological analysis. Subsequently, the rats were sacrificed for histopathological analysis, and the main organs (liver, kidney, and spleen) were collected and analyzed using H&E staining. In addition, skin irritation was monitored following the topical application of MN patches to the dorsal skin of anesthetized mice. The MNs were inserted into the skin using an applicator, and the backing layers were removed after 20 min. The treated skin samples were then harvested at various time points (0, 1, 8, and 24 h) and fixed in 10% formaldehyde solution for histological analysis. After fixation, the tissue samples were dehydrated through a graded series of alcohols, cleared in xylene, and embedded in paraffin. Thin sections (5 μm) were cut from the embedded tissues, mounted on slides, and went through H&E and immunohistochemistry staining of TNF-α. The prepared slides were subsequently observed under the optical microscope to assess potential structural changes and inflammatory responses in the skin.

2.14. *In vitro* effect of NPs and MNs on cancer cells

To evaluate the effect of NIR light on cancer cells treated with Bi_2S_3 NPs, approximately 1.5×10^4 B16F10 cancer cells were seeded in each well of the 96-well plate overnight before the treatment with NPs. The culture medium was then replaced with the fresh culture medium containing Bi_2S_3 NPs with different concentrations (50, 200, and 400 μg mL^{-1}). For each concentration, two groups were tested: one subjected to 10 minutes of NIR irradiation and one without NIR exposure. Afterwards, the samples were incubated at 37 °C for 24 and 48 h. Next, the samples were gently washed using Hank's balanced salt solution (HBSS)–4-(2-hydroxyethyl)-1-piperazine-ethanesulfonic acid (HEPES) (pH 7.4) one time before using a CellTiter-Glo® luminescent assay kit according to the protocol recommended by the manufacturer to measure the viability of cells.[40] A cell culture medium without any tested material was used as a control. All samples were tested in 4 replicates.

Similarly, the same assay was employed to test the effect of PVP, PVP-Bi_2S_3, PVP-SFN, and PVP-Bi_2S_3-SFN MNs on B16F10 cancer cells in the absence and presence of NIR light.

2.15. Combined chemo-PTT of melanoma

The antitumor efficiency of the dissolvable patches was investigated by subcutaneous (SQ) injection of B16F10 cell suspension (10^5 cells) into the backs of male BALB/c mice. When the induced tumor volume grew to 70–100 mm^3 (7–10 days after cell injection), mice were randomly divided into eight groups ($n = 6$): (1) PVP ± NIR, (2) PVP-Bi_2S_3 ± NIR, (3) PVP-Bi_2S_3-SFN ± NIR, and (4) the control group with no MN insertion ± NIR. All treatment groups labeled as PVP, PVP-Bi_2S_3, and PVP-Bi_2S_3-SFN refer to dissolvable MN patches prepared from the respective components. Each mouse received one 10 × 10 MN patch per session, applied on days 0 and 2 at the tumor site. After 20 min, the backing layers were removed and the inserted sites of +NIR groups were exposed to an 808 nm laser light at a power density of 1.5 W cm^{-2} on days 0, 2, and 4. When the temperature reached 48 °C, it remained constant for 5 min while the temperature was recorded with an infrared thermal camera. The body weight and tumor volume ([[(tumor length) × (tumor width)^2]/2) were recorded every 2 days. The size of the tumor was calculated using caliper-based measurement, where length is the largest tumor diameter and width is the perpendicular tumor diameter, in which the height of the tumor is assumed to be equal to its width. The mice were euthanized on day 16 and the tumors were collected and fixed in 10% formaldehyde for histological analysis. All animal experiments were performed according to protocols approved by the Ethics Committee of Zanjan University of Medical Sciences (approval number IR.ZUMS.REC.1400.438).

2.16. Statistical analysis

All the data were expressed as mean ± standard deviation (SD), and experiments were performed at least in triplicate. The data were analyzed using one-way ANOVA, and in all cases, $p \leq 0.05$ denoted significance.

3. Results and discussion

3.1. Characterization of Bi_2S_3 NPs and hydrogel

For prime confirmation of the successful fabrication of Bi_2S_3 NPs, we monitored the color change during the 4-hour synthesis process. The color solution turned from yellow to black, and to examine the characteristics of the synthesized Bi_2S_3 NPs,

its dried black powder was prepared and also photographed, as depicted in Fig. 2a. The size and morphology of the synthesized NPs were examined using TEM and field emission scanning electron microscopy (FESEM, TESCAN MIRA3). According to Fig. 1b and c, the Bi_2S_3 NPs have a smoothly spherical shape and an average particle size of 30–50 nm (Fig. 1d), further extracted by FE-SEM image analysis with the aid of the ImageJ software 1.52 V (National Institutes of Health, USA). To study the colloidal stability of the synthesized NPs, the zeta potential (ζ) was measured (Fig. 1e). When the particles have high negative or positive surface charge, they can resist aggregation or flocculation.[41,42] The obtained ζ of −34.86 mV is an admitted charge to overcome the attraction between the Bi_2S_3 particles. EDX elemental analysis graph of Bi_2S_3 indicated the specified picks for bismuth and sulfur (Fig. 1f). Additionally, based on the weight percentage (wt%) and elemental mapping of the NP sample (Fig. 1g), in addition to Bi (55.89%) and S (15.1%), traces of other elements such as C, N, and O were also detected.

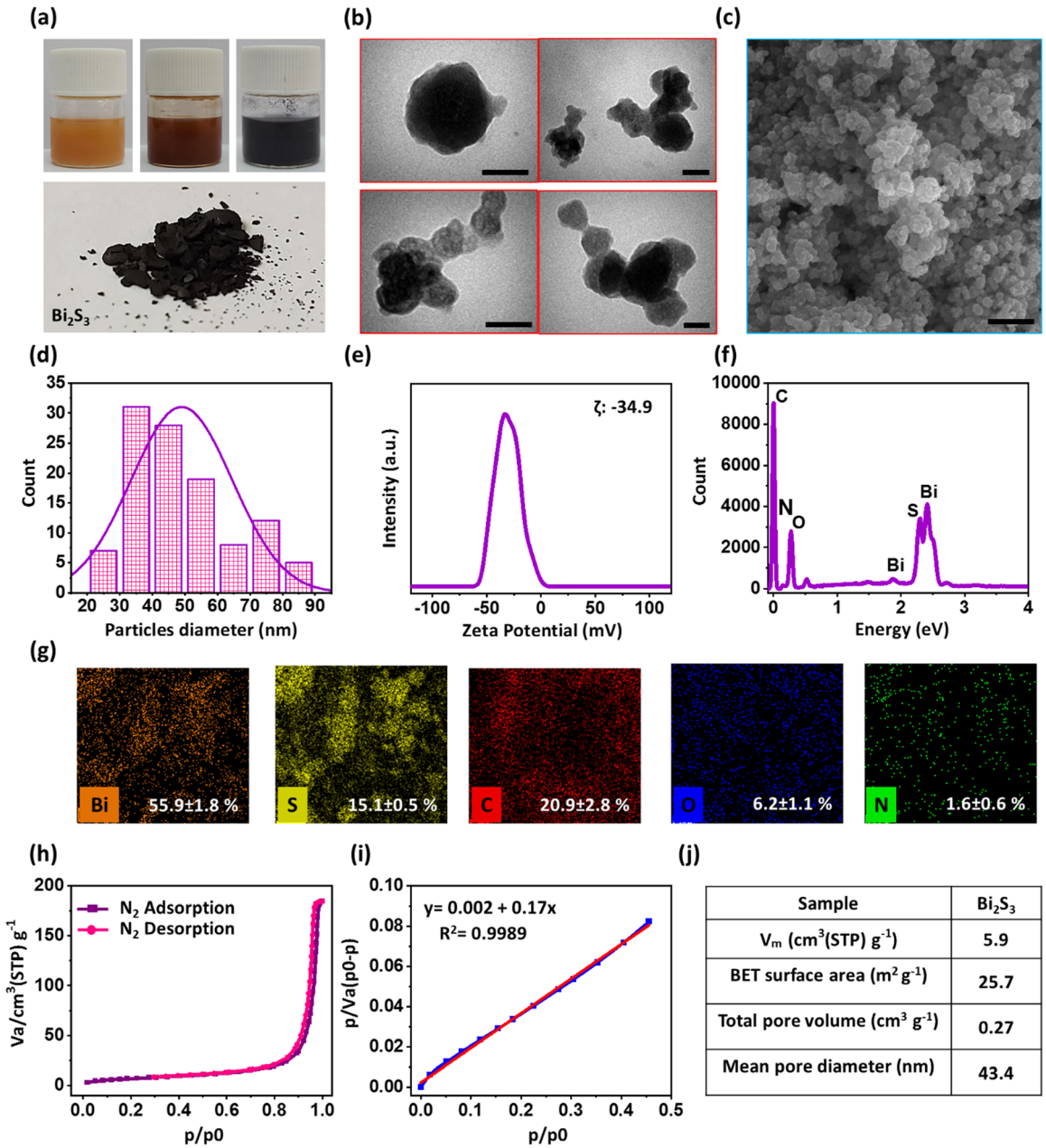

Sample	Bi_2S_3
V_m (cm^3(STP) g^{-1})	5.9
BET surface area (m^2 g^{-1})	25.7
Total pore volume (cm^3 g^{-1})	0.27
Mean pore diameter (nm)	43.4

Fig. 1 Characterization of the synthesized Bi_2S_3 NPs. (a) Representative photographs of the Bi_2S_3 NP solution during the 4 h formation process (top row), and the dried powder of NPs after fabrication (bottom row). (b) and (c) TEM and FE-SEM images of agglomerated Bi_2S_3 NPs (scale bars in the TEM and FE-SEM images represent 100 nm and 1 μm, respectively). (d) Histogram of the NP size distribution according to the TEM images and ImageJ analysis results. (e) Zeta potential intensity distributions for Bi_2S_3 NP. (f) and (g) EDX spectrum, the amount of element in the NP composition (mean ± SD of three replicate samples), and the Bi_2S_3 NP-related elemental mapping. (h) N_2 adsorption–desorption isotherm of the studied NP. (i) BET surface area plot. (j) Presented BET surface area and porosity data of Bi_2S_3 NP.

The presence of N and O can be related to humidity absorbance by the sample and the existence of these elements in the air. The carbon peak observation is also due to the carbon tape used for the EDX analysis.

To identify the pore structure of the synthesized Bi_2S_3 and the specific surface area, the BET analysis was conducted. Based on the IUPAC classification,[43] and the nitrogen sorption isotherm (Fig. 1h), Bi_2S_3 NPs exhibited a type IV isotherm. The hysteresis loop in the range of 0.8–1 of relative pressure (P/P_0) confirmed the mesoporous structure of the NPs. The calculated values for BET SSA, the adsorbed monolayer volume (V_m), total pore volume, and mean pore diameter are represented in Fig. 1j.

To study the chemical structure and functional groups of the compounds, FTIR spectroscopy was assessed (Fig. 2a, the main bands are shown using arrows). In the spectrum of PVP, the bands at 1280 cm^{-1} and 1650 cm^{-1} are related to the stretching vibrations of C–N and C═O, respectively.[44] The broadband at 3200–3500 cm^{-1} can be ascribed to the O–H stretching vibration from surface water absorption, and the stretching band of C–H bonds appears at ~2949 cm^{-1}.[45,46] The synthesized Bi_2S_3 exhibited a metal–sulfur interaction bond at 634 cm^{-1}, demonstrating the successful formation of the Bi_2S_3 NPs. In the region of 1600 cm^{-1} and 3200–3500 cm^{-1}, strong and broad bands are due to O–H bending and stretching vibration of the employed solvent during the NP synthesis, respectively.[47] The spectrum of SFN represents two distinct bands at 3284 cm^{-1} and 3384 cm^{-1} belonging to the N–H stretching vibration of the amide group. The bands at 2927 cm^{-1} and 3078 cm^{-1} are attributed to aliphatic and aromatic C–H stretching groups, respectively. Also, the amide C═O band appears at 1685 cm^{-1}.[48] After adding Bi_2S_3 NPs into the hydrogel, due to the electrostatic interaction between Bi and pair electrons of the carbonyl group in the PVP structure, the band of C═O shifted from 1650 cm^{-1} to 1658 cm^{-1}.[49] After incorporating SFN into the combination of PVP-Bi_2S_3, the final formulation's spectrum shows a broad band in the 3100–3600 cm^{-1} range. This is due to the presence of water, ethanol, and the hydrogen bonding between the carbonyl group of PVP and the H atoms of the carbamide groups of SFN, which covers the N–H peak of SFN. It can be concluded that PVP is a suitable substrate for encapsulating synthesized NPs and SFN since the new bond between PVP,

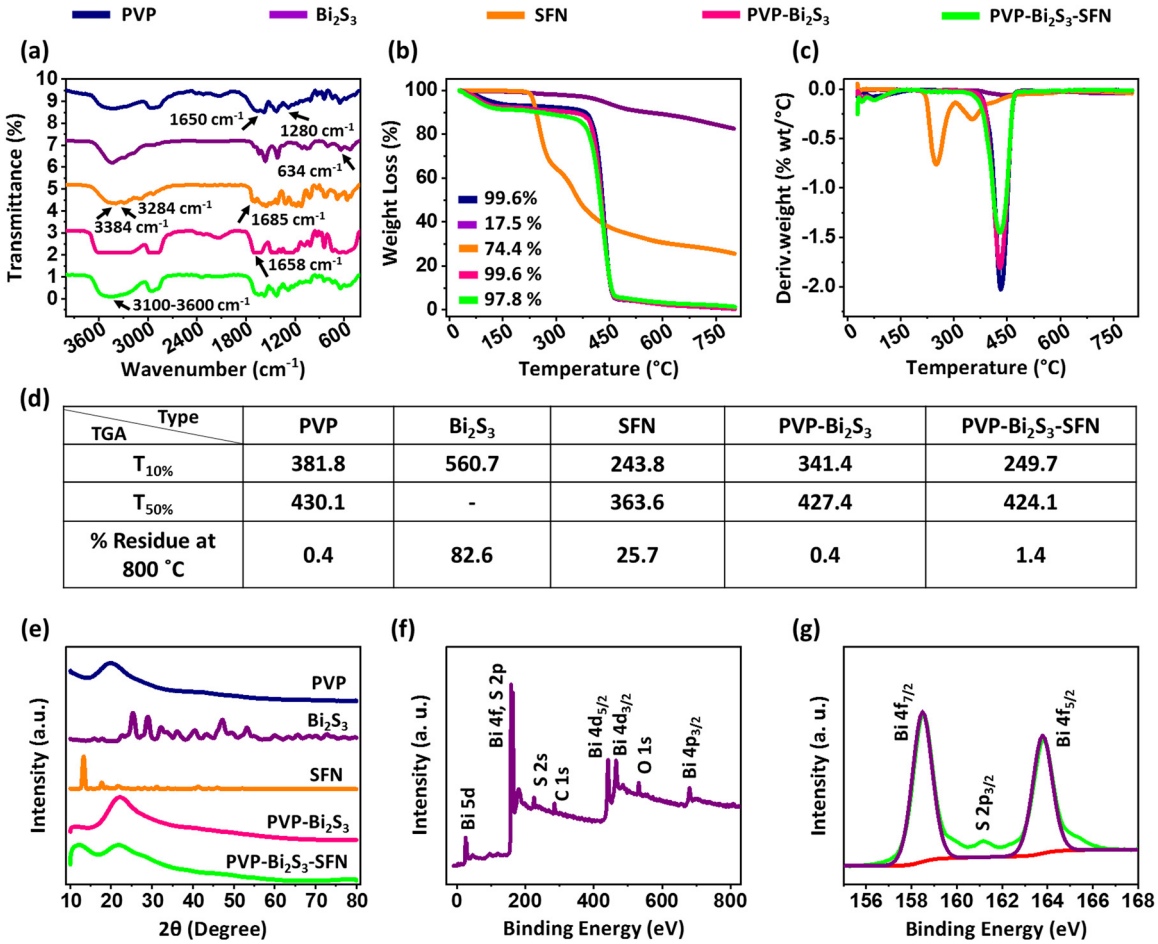

TGA \ Type	PVP	Bi_2S_3	SFN	PVP-Bi_2S_3	PVP-Bi_2S_3-SFN
$T_{10\%}$	381.8	560.7	243.8	341.4	249.7
$T_{50\%}$	430.1	-	363.6	427.4	424.1
% Residue at 800 °C	0.4	82.6	25.7	0.4	1.4

Fig. 2 (a) FTIR analysis. The black arrows in the picture indicate the main peaks of each sample. (b) TGA curve with a representative weight reduction of different samples. (c) DTG thermogram. (d) TGA data at $T_{10\%}$, $T_{50\%}$, and residual percentage at 800 °C. (e) XRD pattern of different samples. (f) Wide-scan XPS spectrum of Bi_2S_3 NPs. (g) XPS spectra of Bi 4f and S 2p core levels.

Bi_2S_3 NPs, and SFN has not formed.[50] The thermal stability and information about the thermal decomposition of the samples were investigated with TGA and derivative thermal gravimetric (DTG), which are shown in Fig. 2b and c. The weight loss of PVP occurred in three stages.[46,51] The initial stage, occurring at approximately 73 °C, is associated with the evaporation of physically adsorbed water, a consequence of the polymer's hygroscopic characteristics. The second stage, observed around 260 °C, involves the thermal cleavage of lactam side groups (pyrrolidone), primarily resulting in the rupture of C–N and C=O bonds. The predominant degradation event occurs at approximately 432 °C, where the scission of the polyvinyl backbone takes place, leading to homolytic cleavage of C–C bonds along the main chain and resulting in rapid depolymerization. Following the temperature of 450 °C, a gradual decomposition of residual char and carbonaceous remnants persists until reaching 800 °C.[52] Bi_2S_3 NPs were almost stable with a little weight loss (17.5%) in the entire temperature range, and this can originate from the removal of moisture and the decomposition of Bi_2S_3 into bismuth metal. SFN showed multiple decomposition stages in an overall 74.39% weight loss.[53] The primary weight loss occurred approximately at 220 °C indicating the primary thermal decomposition of the drug. A second, broader peak appears between ~290 and 420 °C, likely due to stepwise degradation of more stable fragments or intermediate products. This suggests a two-stage decomposition process, even in the absence of excipients or carriers. The results of PVP-loaded NPs/drug are similar to the TGA behavior of pure PVP with nearly 99% weight loss so it can be ascribed to the presence of PVP incorporating Bi_2S_3 NPs and SFN.[54,55] Fig. 2d illustrates the TGA data, which presents the $T_{10\%}$ (temperature at 10% weight loss), $T_{50\%}$ (temperature at 50% weight loss), and the rate of residual content at 800 °C. The structural properties and crystallographic phase of the base materials were analyzed using XRD measurement. From Fig. 2e, PVP with a broad peak at $2\theta \sim 20$ exhibited an amorphous structure, Bi_2S_3 NPs and SFN patterns with sharp diffraction peaks revealed the crystallinity composition, and the PVP-loaded NP/drug is also completely amorphous. Based on the consequential peaks of Bi_2S_3 NPs at scattering angles (2θ) of around 25.4°, 28.9°, and 32.2°, we observed that the obtained NPs are pure orthorhombic Bi_2S_3.[56,57] The crystallite size of Bi_2S_3 NPs was calculated to be 12.4 nm, and for SFN it was 21.3 nm. After embedding SFN and NPs in the PVP hydrogel, their crystal structure, due to the low loading dose, is covered, and just the amorphous peak of PVP was observed. To further verify the composition of synthesized Bi_2S_3, X-ray photoelectron spectroscopy (XPS) was performed. As shown in Fig. 2f, the obtained NPs contain four elements: Bi, S, C, and O. The presence of C and O can be related to atmospheric absorption by the NPs powder or come from reactants in the synthesis process. Two distinct and highest peaks at 158.48 eV and 163.78 eV in the Bi region are assignable to the binding energies of Bi $4f_{7/2}$ and $4f_{5/2}$, respectively (Fig. 2g). Also, the broad peak around 161 eV belongs to the S 2p. Based on the analysis, it can be concluded that the products synthesized were pure bismuth sulfide.[58,59]

3.2. *In vitro* photothermal study

To evaluate the photothermal performance of Bi_2S_3 NPs under NIR irradiation, they were dispersed in solution at varying concentrations (100, 200, and 400 μg mL^{-1}) and exposed to NIR light at 808 nm with three different power densities (0.5, 1, and 1.5 W cm^{-2}). Temperature changes were monitored using a digital thermal imaging camera. It was observed that the temperatures of samples are directly related to both the concentration of NPs and the power of NIR radiation (Fig. 3a). Therefore, an increase in the concentration of NPs or the power density of NIR radiation has resulted in a temperature rise in a time-dependent manner.[60,61] Under exposure to a 1.5 W cm^{-2} NIR laser (808 nm) and a concentration of 400 μg mL^{-1} Bi_2S_3 NPs, the temperature increased by approximately 28 °C after 10 minutes. When exposed to lower intensities of 0.5 W cm^{-2} and 1 W cm^{-2} irradiation, the temperature increased only by 8 °C and 21 °C, at the same concentration and period, respectively. For the Bi_2S_3 NPs with a 100 μg mL^{-1} concentration exposed to a 10-minute NIR irradiation (1.5 W cm^{-2}, 808 nm), the temperature increased to 47 °C. The temperature of the Bi_2S_3 NPs solution with a concentration of 200 μg mL^{-1} was raised to 51 °C, and the Bi_2S_3 NPs at 400 μg mL^{-1} could generate heat up to 54 °C. When the temperature of tumor cells exceeds 48 °C, it can cause irreversible damage to the cellular protein and DNA, thus effectively ablating the tumors,[62,63] which can be achieved using our developed MNs using 400 μg mL^{-1} of the NPs as the optimal concentration. The photothermal efficiency of Bi_2S_3 NPs was even enhanced by embedding them into PVP hydrogel because of a compact network, improved dispersion, and stability of NPs. The temperature changes of PVP-Bi_2S_3, and PVP-Bi_2S_3-SFN hydrogels were investigated under a 10-min NIR laser at 808 nm with different power densities (Fig. 3b). At a power density of 0.5 W cm^{-2}, no significant increase or difference in temperature was seen between formulations. The temperature of PVP-Bi_2S_3 and PVP-Bi_2S_3-SFN reached 52.3 and 47 °C, respectively, when exposed to NIR light with a power of 1 W cm^{-2} for 10 min. At the laser power of 1.5 W cm^{-2}, the temperatures reached 64.4 and 62.3 °C for these two samples. Fig. 3c shows thermal images of the final formulation in solution and hydrogel state with an optimized concentration of Bi NPs (400 μg mL^{-1}) and power density of NIR laser (1.5 W cm^{-2}). The photostability of the photothermal agent was meticulously assessed through five consecutive heating and cooling (On and Off) cycles with persistent temperature variations observed throughout all cycles (Fig. 3d). The PVP-Bi_2S_3-SFN hydrogel, as a final formulation, exhibited a high and efficient photothermal conversion ability (η) after a 10-minute NIR irradiation (1.5 W cm^{-2}), followed by natural cooling back to room temperature (Fig. 3e). The calculated η was 49% (Fig. 3f). High photothermal conversion efficiency and excellent photothermal stability of synthesized Bi_2S_3 NPs lay the foundation for their application in PTT of melanoma.

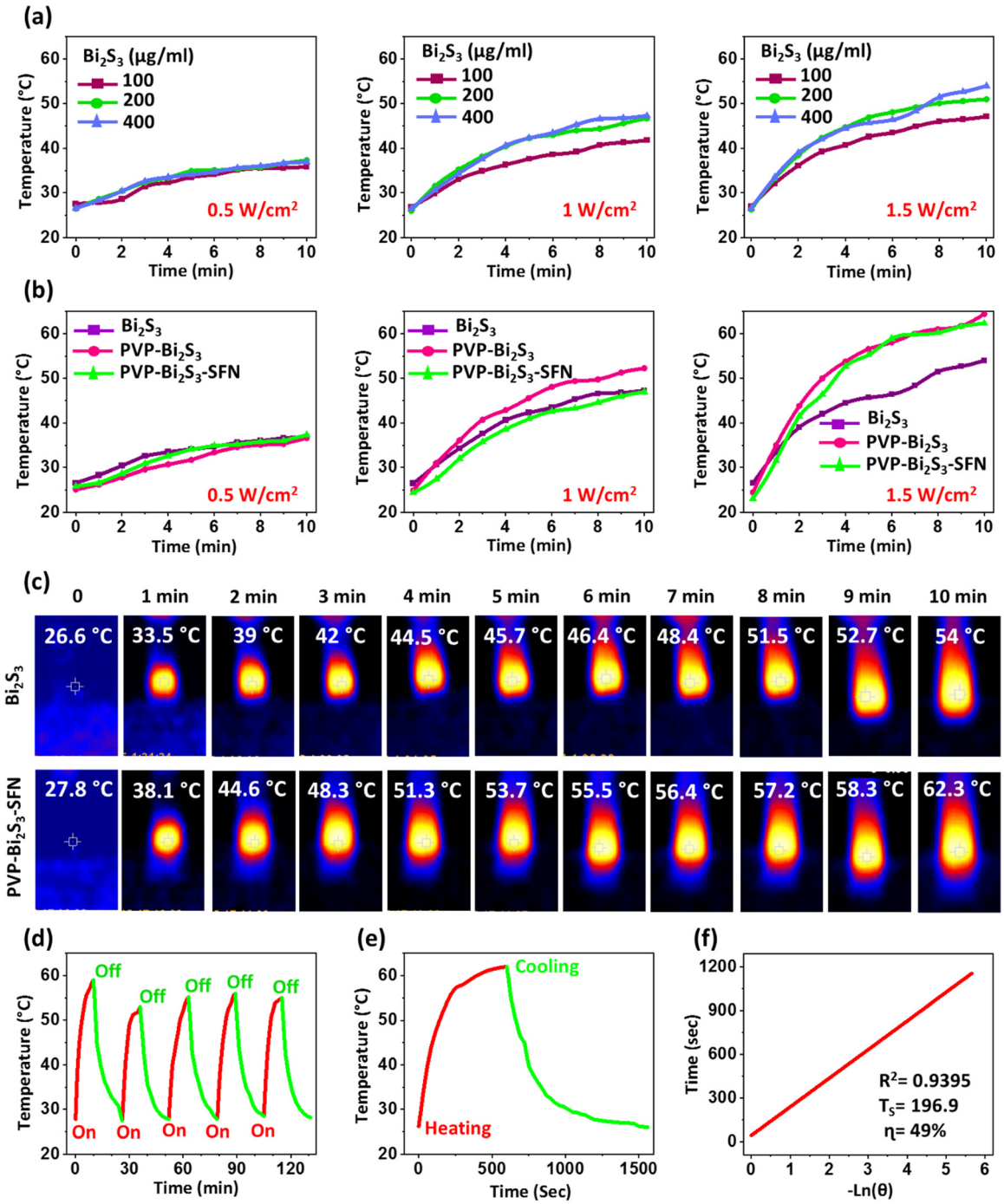

Fig. 3 Photothermal behavior of Bi_2S_3 NPs. Temperature variation of an (a) aqueous dispersion of Bi_2S_3 NPs with different concentrations under 808 nm NIR irradiation for 10 min (0.5, 1, and 1.5 W cm^{-2}), and (b) aqueous dispersion of Bi_2S_3 NPs (400 μg mL^{-1}) and hydrogel loaded Bi_2S_3 NPs (PVP-Bi_2S_3, PVP-Bi_2S_3-SFN with Bi_2S_3 concentration of 400 μg mL^{-1}) under different NIR laser power densities (808 nm, 10 min). (c) Infrared thermal images of an aqueous dispersion of Bi_2S_3 NPs (400 μg mL^{-1}) and PVP-Bi_2S_3-SFN hydrogel under 1.5 W cm^{-2} NIR irradiation (808 nm) within 10 min. (d) Temperature change curve of Bi_2S_3 NPs intra hydrogel matrix (PVP-Bi_2S_3-SFN) during the five circles of NIR laser on/off (808 nm, 1.5 W cm^{-2}). (e) Heating and cooling curve of PVP-Bi_2S_3-SFN hydrogel under NIR irradiation (808 nm, 1.5 W cm^{-2}, Heating: 10 min, Cooling: 15 min). (f) The linear plot of cooling time *versus* $-\ln(\theta)$.

3.3. Hemolysis and *in vitro* PTT effect on cell viability

The hemocompatibility of the materials was tested using an *in vitro* hemolysis assay. Human RBCs were exposed to the hydrogels at different concentrations (50, 100, 200, 400 μg mL^{-1}) for 1, 4, 8, 24, and 48 hours. The results showed no hemolysis of the erythrocytes in contact with PVP, PVP-Bi_2S_3, and PVP-Bi_2S_3-SFN hydrogels (Fig. 4a). However, after 24 and 48 hours of incubation, unloaded Bi_2S_3 NPs induced blood toxicity, more than the standard level of hemolysis ratio (5%).[64] The observed hemolysis at later time points may be due to prolonged interactions

between NPs and the membrane, leading to structural disruption of the erythrocyte membrane. This disruption could be mediated by ROS generation or mechanisms driven by surface charge, as previously reported for similar metal sulfide nanostructures.[65,66] Based on the photographs of the investigated samples that are presented in Fig. 4b, it was observed that the supernatant of the hydrogel groups was colorless and similar to the transparent solution of the negative control (PBS; pH 7.4). The blood compatibility of Bi_2S_3 NPs after loading in PVP hydrogel can be related to the reduced contact of Bi_2S_3 NPs with erythrocytes. Overall, these assays highlighted the favorable hemocompatibility of the prepared hydrogels for biomedical applications.

The cytotoxic effect of the NPs and the final formulations under NIR light was also investigated on B16F10 cancer cells. As illustrated in Fig. 4c and d, cells treated with various concentrations of Bi_2S_3 NPs at 50, 200, and 400 μg mL^{-1} exhibited a dose-dependent reduction in viability when subjected to NIR irradiation (808 nm, 1.5 W cm^{-2} for 10 min) at both 24 and 48 h post-treatment. In contrast, no significant cell death was observed in any groups that did not receive laser irradiation, demonstrating the biocompatibility of Bi_2S_3 NPs. Furthermore, the viability of the cells decreased meaningfully from approximately 88% at 50 μg mL^{-1} to around 7% at 400 μg mL^{-1} as a result of NIR exposure. In addition, B16F10 cells were treated with various PVP-based hydrogels to evaluate cell toxicity related to chemotherapy, PTT, and combination therapy, with and without NIR irradiation (808 nm, 1.5 W cm^{-2} for 10 min) after a 24-hour incubation period (Fig. 4e). The results for PVP (±NIR) and PVP-Bi_2S_3 (Bi_2S_3: 400 μg mL^{-1}, −NIR) demonstrated no significant difference in cytotoxicity compared to the control group (±NIR). However, upon NIR irradiation, the viability of PVP-Bi_2S_3-treated cells declined to approximately 60%, indicating the photothermal effectiveness of the synthesized NPs in inducing cancer cell apoptosis. In the case of PVP-SFN, whether exposed to NIR or

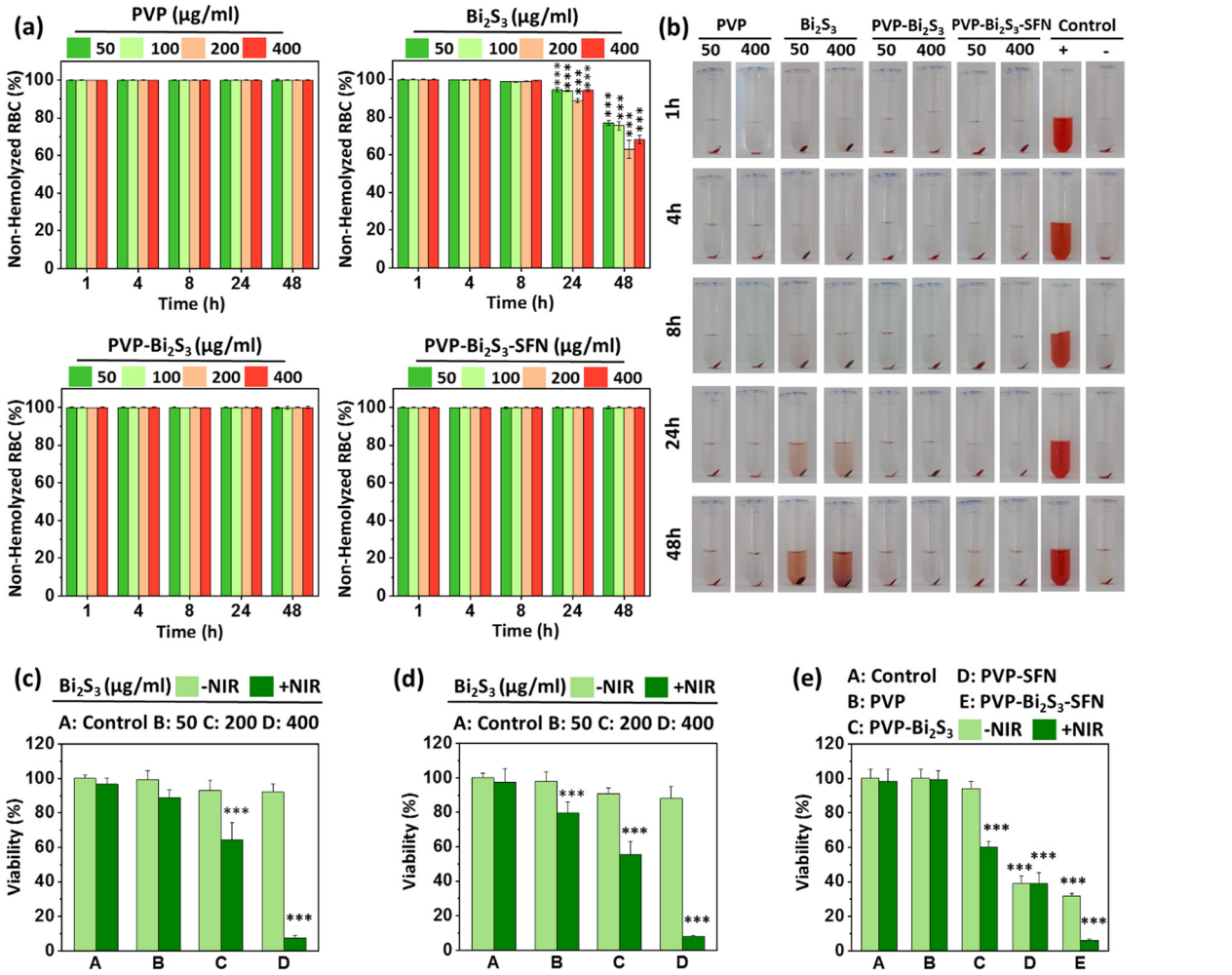

Fig. 4 (a) Time and concentration-dependent hemocompatibility study of PVP, Bi_2S_3, PVP-Bi_2S_3, and PVP-Bi_2S_3-SFN. Data are presented as mean ± SD (N = 4), ***$p < 0.001$ *vs.* negative control group. (b) The photographs of RBC samples exposed to PBS (negative control), DIW (positive control), and different concentrations of PVP, Bi_2S_3, PVP-Bi_2S_3, and PVP-Bi_2S_3-SFN (μg mL^{-1}) at 1, 4, 8, 24, and 48 h incubation time. The viability of B16F10 cells treated with the Bi_2S_3 NPs at concentrations of 50, 200, and 400 μg mL^{-1} (±NIR) at (c) 24 h and (d) 48 h. The irradiation for the +NIR groups was at 808 nm, 1.5 W cm^{-2} for 10 min. Data are expressed as mean ± SD (N = 4) and *** represents $p < 0.001$ *vs.* control group (−NIR). (e) The viability of B16F10 cancer cells after treatment with different hydrogels and subsequent exposure to NIR (808 nm, 1.5 W cm^{-2} for 10 min) at 37 °C.

not, there was a 60% killing effect, reflecting the potential of SFN to suppress cancer cell growth, similar to the PVP-Bi_2S_3-SFN group without NIR. The cumulative effect of chemotherapy and PTT was evident in the PVP-Bi_2S_3-SFN group following 10 min of laser irradiation, resulting in cell viability of only 6%.

3.4. Characterization of the dissolvable MN

The SEM and microscopic images of blank and loaded MNs (Fig. 5) depicted that the height of each needle was around 640 μm, with a 290 μm base width and a 4 μm tip diameter, which is sharp enough to insert into the skin.[67] The shorter height of formed needles than the main height of the mold can be attributed to polymer backbone shrinkage and water evaporation during the drying process.[68,69] The elemental analysis of PVP-Bi_2S_3 confirms the presence of Bi and S in the sample, while the addition of SFN is responsible for the F and Cl detection in the structure of PVP-Bi_2S_3-SFN MNs (Fig. 5b and c). The consistency of these observations with the previous results indicates the successful loading of Bi_2S_3 NPs and SFN into the PVP MNs.

3.5. Mechanical studies and drug loading

The mechanical strength required to penetrate the stratum corneum is a key feature needed for effective drug delivery by MNs.[70,71] Pyramidical MNs, compared to the conical shape, represent better pressure resistance,[69] which was the reason for creating such MNs in this study. To achieve skin penetration, the force applied to the MN tip must exceed the force needed to

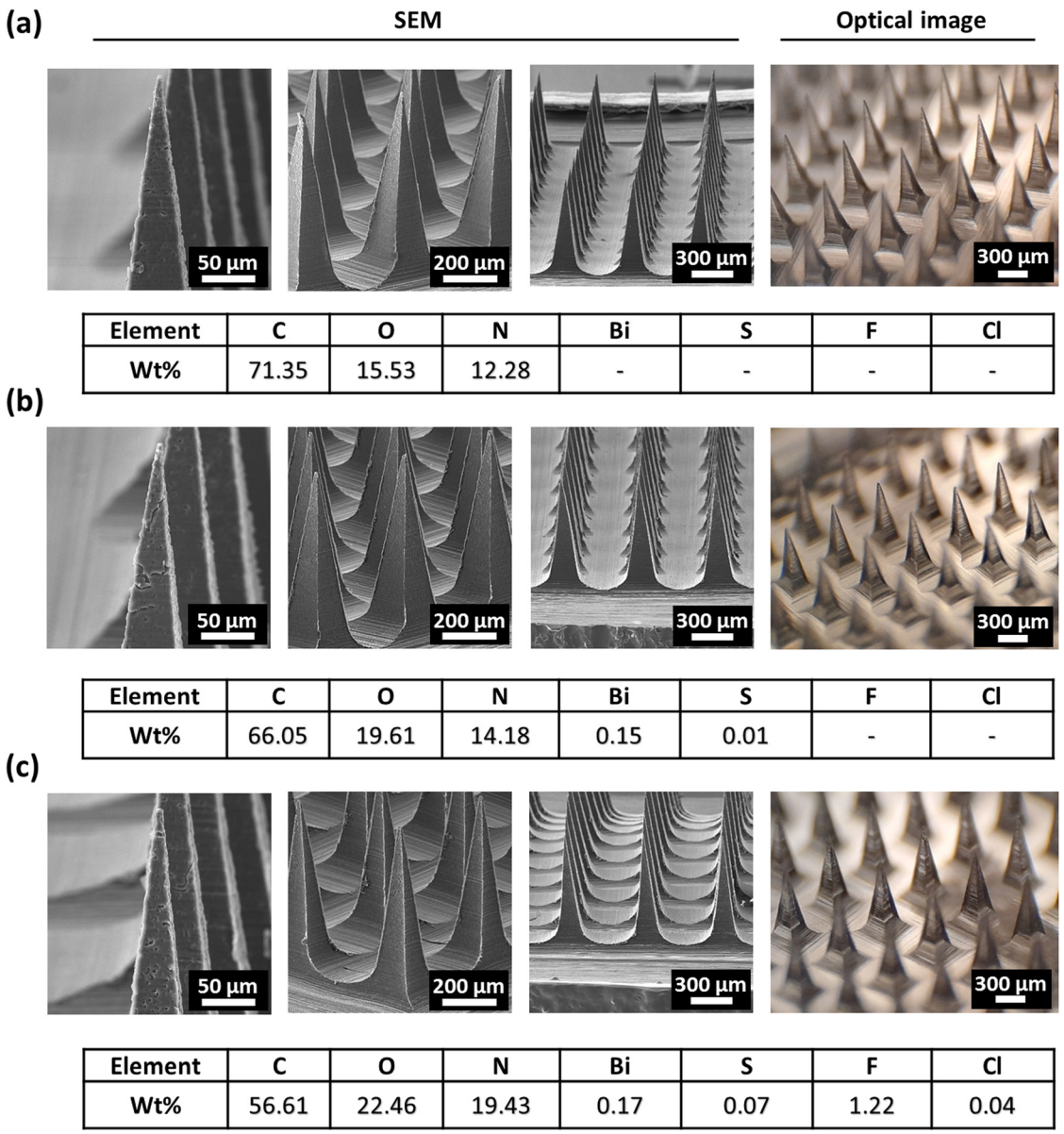

Element	C	O	N	Bi	S	F	Cl
Wt%	71.35	15.53	12.28	-	-	-	-

Element	C	O	N	Bi	S	F	Cl
Wt%	66.05	19.61	14.18	0.15	0.01	-	-

Element	C	O	N	Bi	S	F	Cl
Wt%	56.61	22.46	19.43	0.17	0.07	1.22	0.04

Fig. 5 SEM, optical microscopic image, and EDX data of (a) PVP, (b) PVP-Bi_2S_3, and (c) PVP-Bi_2S_3-SFN MN patches. Each group includes images labeled as "SEM" and "Optical," along with the corresponding EDX data.

pierce the skin, without causing MN fracture during insertion. The mechanical properties of MNs can be affected by different factors, such as the needle geometry, length, base width, tip diameter, and composition of the MN patch.[72,73] To explore the rigidity of the developed MN patch, a universal testing machine with axial compression against the fixed patch on the steel plate was operated. According to Fig. 6a, which represents the reduction height of needles *versus* applying force (15–73 N), it was observed that increasing force results in a decrease of MN height without breakage. The force–displacement curve shown in Fig. 6b indicates that the mechanical behavior of PVP MN has been improved by loading Bi_2S_3 NPs and SFN, which suggests that the presence of the NPs and drug has a reinforcing effect on the polymer structure. The loaded components did not influence the mechanical behavior at forces under 0.5 N per needle; however, they demonstrated a reinforcing effect when the applied force exceeded this level. The displacement of MNs increased with pressure elevation, and a sudden drop in force was observed at the fracture force of ≈0.73 N per needle. This is higher than the force needed for effective penetration of MNs to the skin, resulting in successful transdermal drug delivery.[74] Fig. 6c demonstrates SEM and optical images of PVP-Bi_2S_3-SFN needles after being subjected to different forces.

The skin insertion capability of the MNs was visualized using an 8-layer Parafilm M® sheet as a skin phantom model.

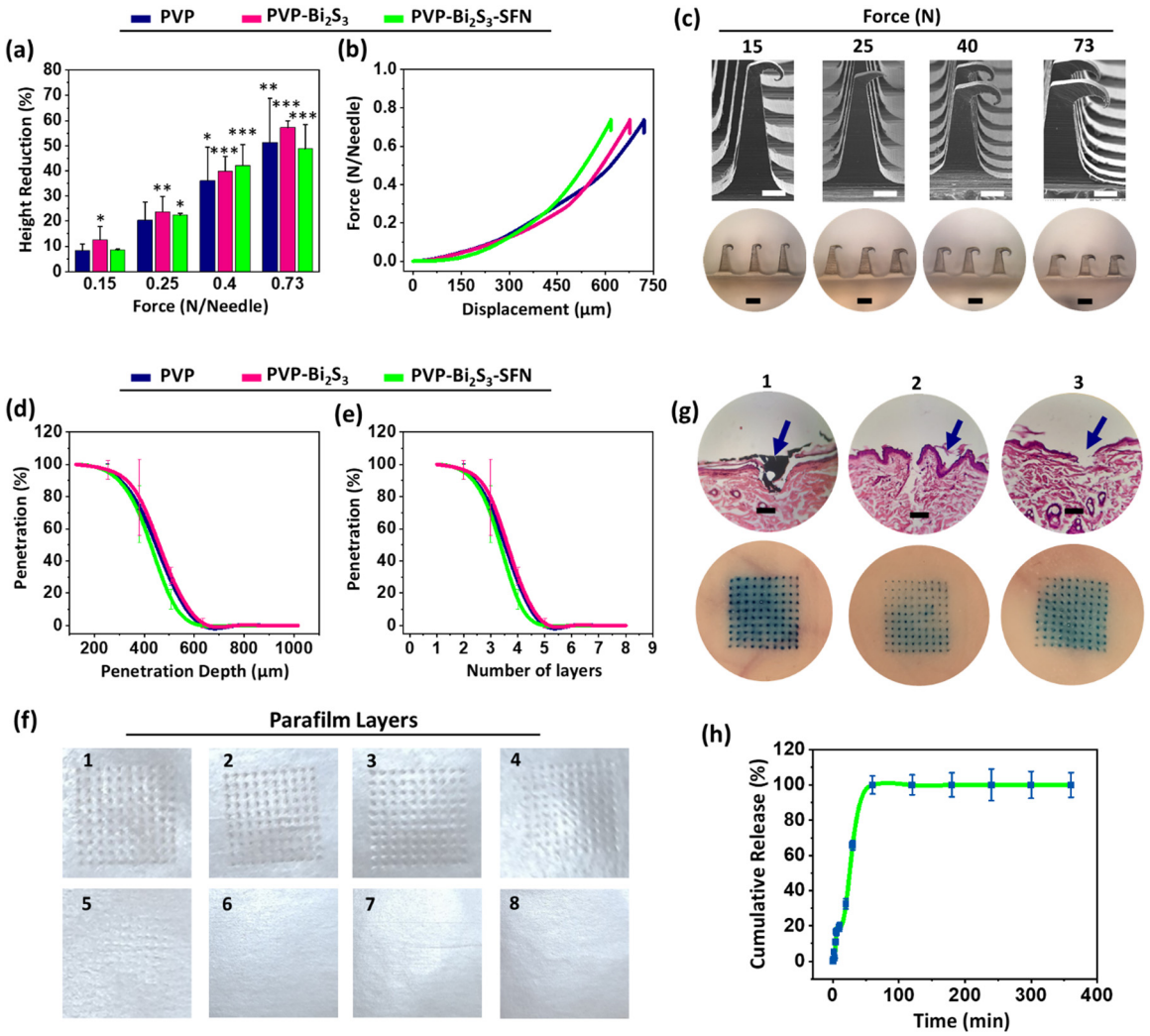

Fig. 6 Mechanical behavior of the fabricated MN arrays. (a) The reduction height of MNs under different stress conditions (mean ± SD, N = 3, and $*p < 0.05$, $**p < 0.01$, and $***p < 0.001$), (b) force–displacement curves showing sudden force drops corresponding to structural failure of different MN matrices, and (c) the morphology of PVP-Bi_2S_3-SFN needles shown using SEM and optical microscopic images after applying different compressive forces (scale bars in the SEM and optical images represent 100 μm and 300 μm, respectively). MN insertion study *in vitro*. (d) Insertion depth of MN arrays and percentage of holes created in the 8-layer Parafilm M® with different types of MN arrays (mean ± SD, N = 3), (e) penetration degree in each layer of Parafilm M® (mean ± SD, N = 3), (f) photographs of unfolded Parafilm M® layers after insertion of the PVP-Bi_2S_3-SFN MN patch, and (g) H&E staining and related photographs of inserted rat cadaver skin to express insertion performance of trypan blue-loaded MN patches. Blue arrows in the H&E images show the skin puncture site after needle insertion. 1: PVP, 2: PVP-Bi_2S_3, and 3: PVP-Bi_2S_3-SFN. Scale bar: 300 μm). (h) Cumulative release profile of SFN (mean ± SD, N = 3).

Based on the thickness of the layers, after insertion of each patch with thumb pressure, the simulated penetration depth to the epidermis area of skin was determined, showing no significant difference between different MNs (Fig. 6d and e). The photos of each layer (PVP-Bi_2S_3-SFN patch), presented in Fig. 6f, confirmed that no penetration occurred in the layers 6, 7, and 8 of the Parafilm M® sheet. Over 70% of the needles penetrated up to a depth of 381 μm (layer 3), which clearly demonstrates the mechanical robustness of the fabricated MNs in effectively overcoming the stratum corneum barrier (10–15 μm thickness).[75] To further study the *in vitro* insertion of the MNs, they were loaded with trypan blue dye and inserted into rat cadaver skin. The insertion ratio was observed, and the results were confirmed by H&E staining of the inserted skin. The histological images (Fig. 6g) demonstrated the creation of micropores on the skin and confirmed successful skin penetration by MNs. Additionally, photographs of the skin's surface revealed the presence of blue spots (10 × 10) corresponding to the full insertion of the needles into the skin. According to the results, the insertion depth was about 300 μm, which is enough to overcome the stratum corneum but shorter than the original height of the MNs. This could be ascribed to the elasticity of skin,[33] and the fast dissolving of MNs' tips after adsorption of physiological fluid.

The amount of SFN loaded in each MN array was calculated to be 19 ± 1 μg. The drug release monitoring indicated that about 32% of the drug was released cumulatively within 20 min and 100% of the drug was released in 60 min (Fig. 6h). During the analysis, the needles were observed to dissolve completely in 1 min and the entire patch dissolved after 35 min. This suggests the patch can appropriately deliver the drug.

3.6. Dissolution rate and *ex vivo* penetration depth

To reveal the *in vivo* dissolution profile of the dissolvable MNs, the prepared patches were applied onto both rat and mouse dorsal skin. An applicator was used to insert the MN arrays into the skin with and without using a hard support placed under the skin. The MN patches were removed at different intervals, and the residual needles were observed with SEM and optical microscopy (Fig. 7a and b). When MNs were inserted into rat

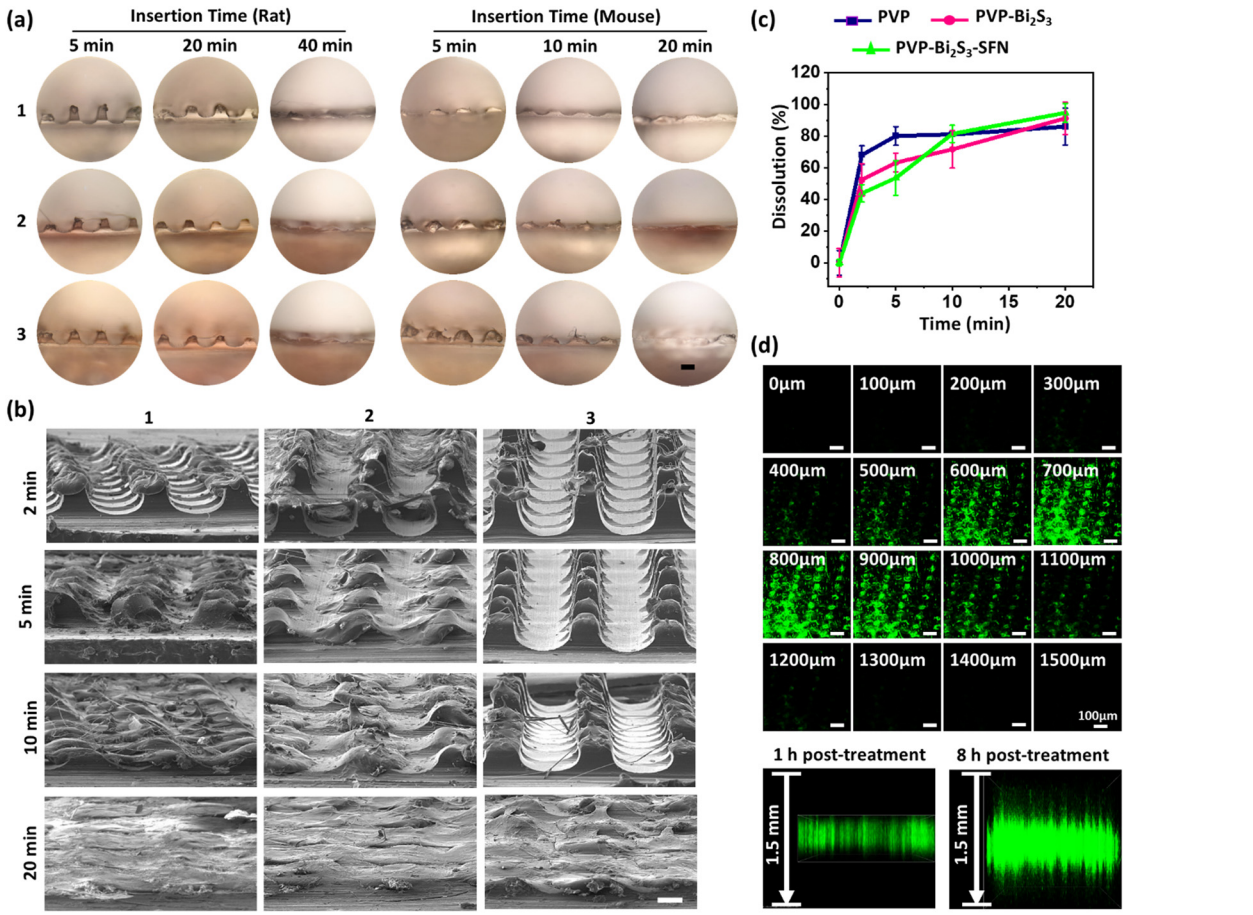

Fig. 7 (a) Optical microscopic images of dissolved needles (1: PVP, 2: PVP-Bi_2S_3, 3: PVP-Bi_2S_3-SFN) after insertion into the rat and mouse skin and lid method at different time points. Scale bar: 300 μm. (b) The dissolution behavior of fabricated needles after insertion into the mice skin within 2, 5, 10, and 20 min was observed by SEM (through an applicator and lid method). Scale bar: 200 μm. (c) The dissolution rate of applied MN arrays on the mice's skin with different matrices and the lid method (mean ± SD, N = 3). *Ex vivo* transdermal drug delivery potential of FITC-loaded PVP-based MN across the rat skin. (d) Cross-sectional confocal microscopic images of micropores created at varying depths over 8 h and 3D-reconstruction images within 1 and 8 h post-administration.

skin supported by a hard backing beneath the skin, 76% of the MNs dissolved within 20 minutes, and complete dissolution occurred by 40 minutes. In contrast, without the hard backing support under the skin, the MNs showed a 58% reduction in height at 20 minutes and a 96% reduction at 40 minutes. These results suggest that using a hard support beneath the skin facilitates more effective needle insertion. The higher permeability and lower thickness of mouse skin, relative to rat skin, resulted in a more rapid dissolution rate. Based on the microscopic images, the residual height, and dissolution curves *versus* time for the patches insertion with the hard support on the mice skin (Fig. 7c), the PVP needles had an 80% reduction in height after 5 min, while loaded MNs demonstrated a lower dissolution rate of nearly 63% and 53% for PVP-Bi_2S_3 and PVP-Bi_2S_3-SFN, respectively. Nearly complete dissolution was observed within 20 minutes across all types of patches. On the other hand, without the hard support under the skin, the residual needle height for PVP, PVP-Bi_2S_3, and PVP-Bi_2S_3-SFN MNs was 44%, 32%, and 33% in 40 min, respectively. It can be concluded that the loaded components did not highly affect the dissolution process in this case, and the dissolution rate was slower. In the following studies, the insertion was done with the backing support and a time of 20 min was chosen for the MN dissolution in the skin.

The depth to which encapsulated cargo can penetrate the skin was determined *ex vivo* for MNs loaded with FITC. The MNs were applied to shaved and anesthetized dorsal rat skin for 20 min before removal. The treated skins were imaged using confocal microscopy. The confocal cross-sectional images after 8 h of treatment are shown in Fig. 7d, along with a 3D reconstruction of Z-stack confocal images after 1 and 8 h post-administration. The penetration depth increased from 500 μm to 1500 μm over 8 hours. Overall, the insertion study confirmed that the drug penetrated deeper into the skin than the original insertion depth of the MNs. The dissolution and release successfully occurred, and the fabricated MN patch could overcome the skin barriers and deliver the model cargo to the dermis layer.

3.7. Skin irritation study and *in vivo* toxicity effect

The MN insertion method effectively creates micropores on the skin, which inevitably leads to an immune response that attracts immune cells and inflammatory factors to the epidermis and dermis.[76] Skin irritation was tested by applying the MNs to the dorsal skin of an anesthetized mouse. The skin samples were harvested at 0, 1, 8, and 24 h after the treatment. The treated skin exploration using histopathological and cross-sectional images (H&E staining) immediately after removing the patches at 0 h showed no skin irritation (refer to Fig. 8a). However, after 1 h, the inflammatory cell infiltration increased in the groups treated with loaded MNs and then decreased over time, which can be attributed to the anti-inflammatory effect of Bi_2S_3 NPs.[77] Moreover, the skin site where the patches were inserted healed and recovered within one day. The immunohistochemistry results of the treated skin (TNF-α staining) were consistent with the H&E staining images. As shown in Fig. 8b, TNF-α expression was observed during 8 h and then declined after 24 h. No infection or abnormal change on the skin surface of mice was observed during the study.

The serum blood analysis and pathological examination were further performed to evaluate the *in vivo* biocompatibility of the introduced MN-patch. First, the animals were treated for 5 days, and then the blood and main organs were collected to investigate biochemical parameters, blood routine, and histological analysis. In comparison to the control group, the biochemical factors like total protein (TP), albumin (ALB), phosphor (Ph), lactate dehydrogenase (LDH), liver function markers such as ALP (alkaline phosphatase), ALT (alanine transaminase), and AST (aspartate aminotransferase) and the kidney function markers including blood urea nitrogen (BUN) and creatinine (Cr) levels in the treated groups remained within the normal range with no significant changes (Fig. S1, ESI†). However, there was an exception in the BUN count for the PVP-Bi_2S_3-SFN group. Also, there was no obvious change in the blood routine values (RBC, WBC, PLT, LYMP, HGB, MONO, NEUT, HCT) as shown in Fig. 8c. Furthermore, the H&E staining results of the kidneys, liver, and spleen displayed no significant inflammation, tissue pathological damage, or lesions in the treatment groups compared with the control group (Fig. 8d). Given the *in vitro* and *in vivo* results, we can conclude that the prepared patch is safe for melanoma therapy.

3.8. *In vivo* photothermal effect

Motivated by high *in vitro* photothermal conversion potential, the photothermal behavior was studied to develop the efficiency of *in vivo* PTT. The prepared MN patches were applied on the shaved dorsal skin of mice for 20 min. Subsequently, the patch was peeled off and the inserted site of skin was irradiated by NIR laser (1.5 W cm^{-2}, 808 nm) for 10 min and the temperature variation was recorded with the infrared imaging camera (Fig. 8e). The injected mice using PVP MNs (without the photothermal agent) showed a 14 °C temperature increase related to light-skin interaction. In contrast, in the treated mice with Bi_2S_3 loaded MNs groups (PVP-Bi_2S_3 and PVP-Bi_2S_3-SFN patches), the local temperature in 5 min reached higher than 42 °C, and within 10 min irradiation increased to nearly 50 °C which was sufficiently high for tumor cell ablating. Overall, the findings confirmed the successful therapeutic agent release of the produced MN through transdermal drug delivery and the photothermal conversion ability of synthesized Bi_2S_3 NPs to ideal PTT.

3.9. Combination therapy effect on melanoma

The anticancer potential of MN-mediated photothermal and chemotherapy was assessed on the established melanoma model through subcutaneous B16F10 bearing BALB/c mice. The mice were randomly divided into 8 groups (6 animals per group) and labeled as the control, PVP, PVP-Bi_2S_3, and PVP-Bi_2S_3-SFN with or without NIR exposure. The control group consisted of untreated mice bearing tumors. To perform combination therapy in the treatment groups on days 0 and 2 of the treatment process, each mouse was administrated intertumorally

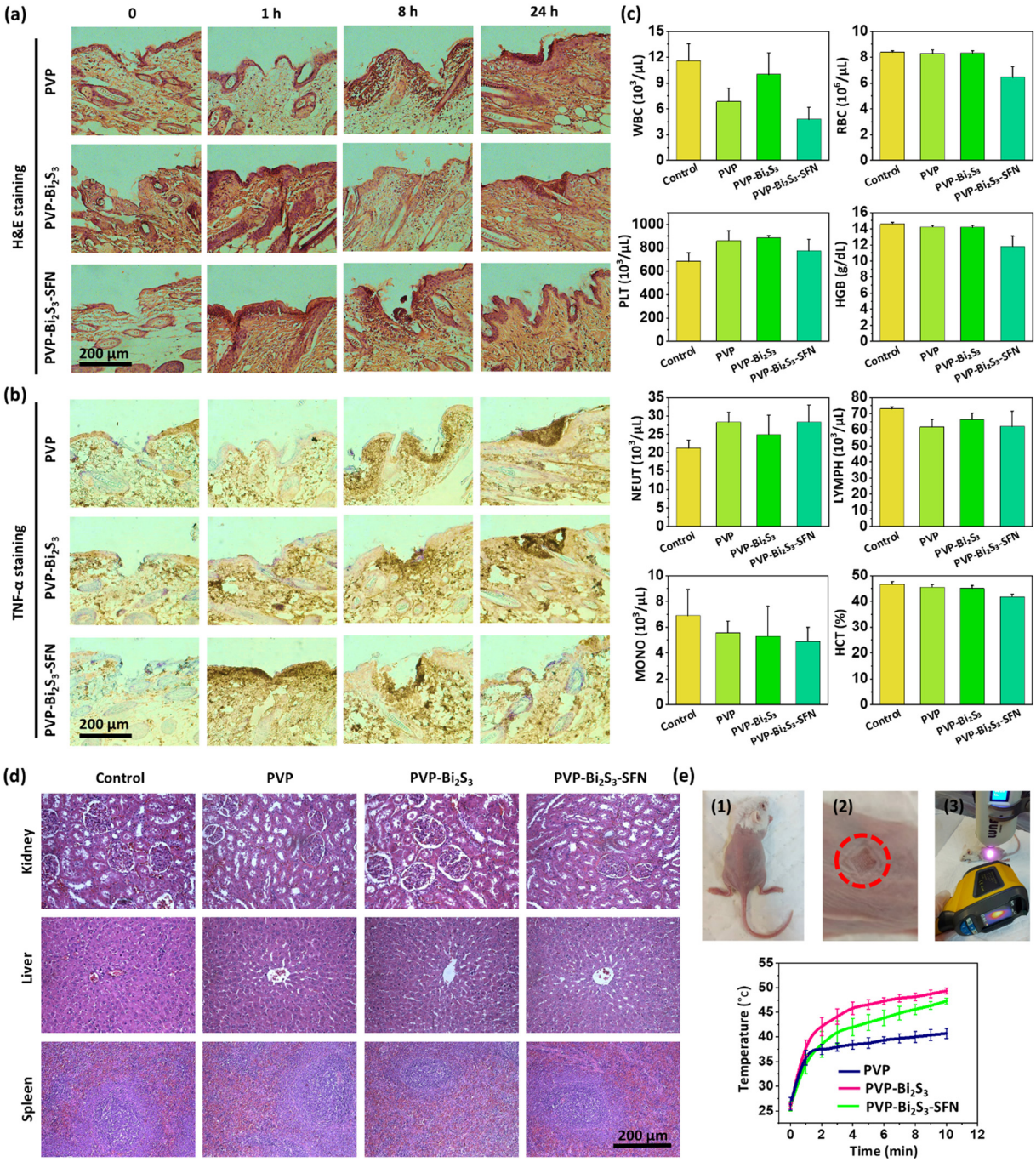

Fig. 8 *In vivo* toxicity evaluation. (a) H&E staining and (b) TNF-α staining of treated skin with the MN systems during 24 h. (c) Effect of MN application (three times) on blood factors level during a 5-day treatment process. Effects of MN application (three times) on metabolic biochemical factors during a 5-day treatment process are shown in Fig. S1 (ESI). Results are presented as mean ± SD (N = 4). (d) Histopathological change in the kidneys, liver, and spleen of treated animals. Photothermal potency of Bi_2S_3-loaded MNs in comparison to the PVP MN, *in vivo*. (e) Representative images of MN insertion steps and NIR irradiation: (1) the mouse skin was shaved, and the MN arrays were inserted by an applicator and using a lid, (2) skin puncture marks, and (3) NIR laser exposure (808 nm, 1.5 W cm^{-2}) at the inserted site, and the temperature elevation profile for 10 min (mean ± SD, N = 3).

with the MN patch for 20 min and subsequently, in the +NIR groups, was exposed under the laser irradiation. Implementation of PTT at 42–45 °C, and in some reports even below 48 °C, is known as mild temperature tumor therapy, which can induce reversible apoptosis in cancer cells without causing irreversible thermal damage to surrounding tissues.[78,79] However, this mild temperature therapy has poor therapeutic efficiency and can also lead to tumor thermal resistance. If the temperature exceeds the mild temperature range, it can cause tumor disruption by increasing blood vascular permeability, necrosis, and irreversible DNA and protein damage. Meanwhile, it is crucial to maintain a careful balance between the temperature used for therapy and its

potential effects on both cancerous and healthy cells. Exceeding the temperature over 48 °C can prompt negative results on healthy tissue, making it imperative to be cautious when performing PTT.[79,80] Hence, in this research, the adequate temperature for tumor challenge and minimizing injury to healthy tissues was determined at 48 °C. Considering the extreme potential of the MNs containing Bi_2S_3 NPs to increase the tumor temperature higher than the mild temperature range when the tumor heat

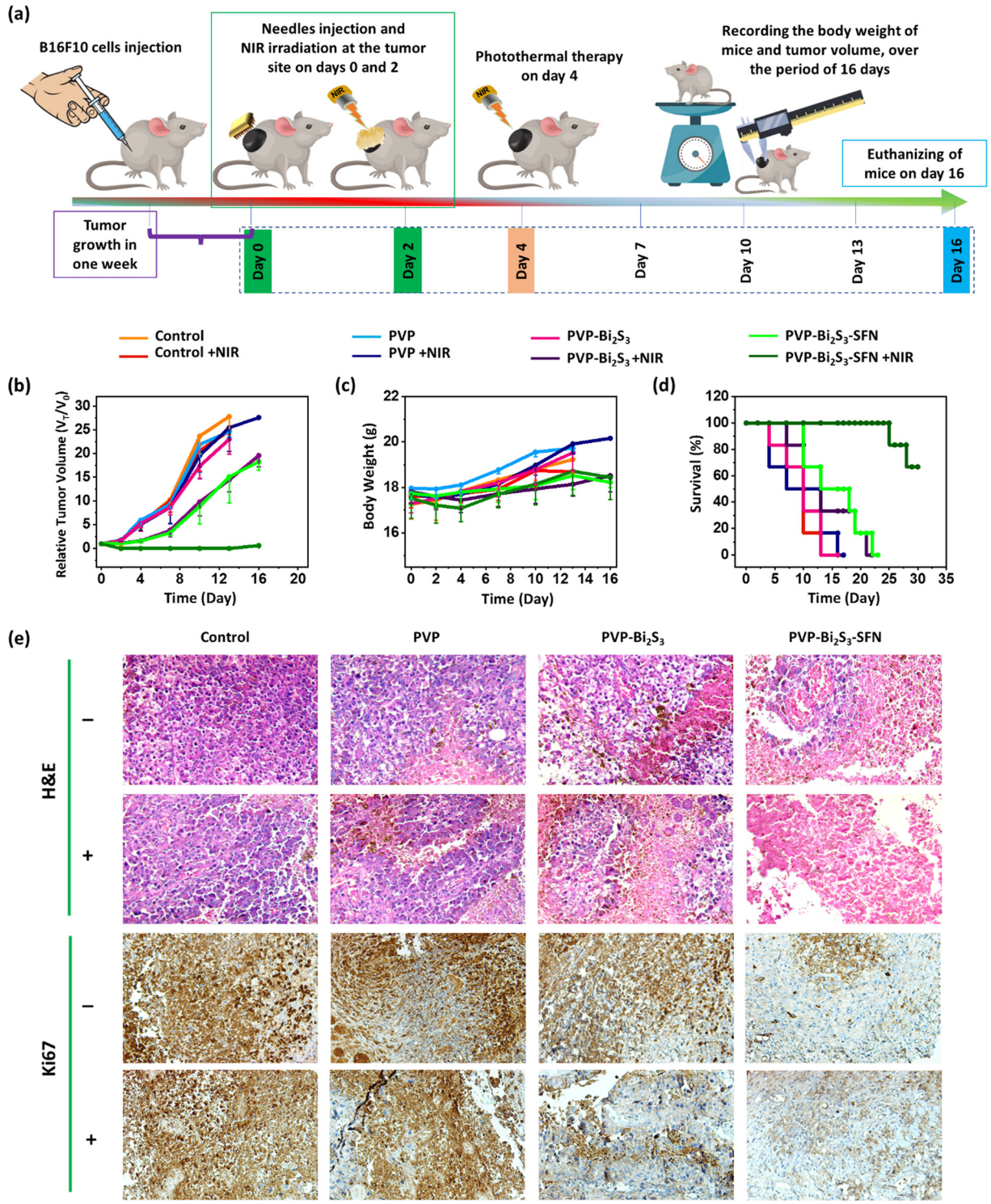

Fig. 9 (a) Illustration of the treatment plan on different days of melanoma combination therapy. (b) Relative tumor volume curve of intervention treatments. (c) Body weight of mice in each group during the 16-day treatment. (d) Survival rate in the experimental mice. (e) H&E and Ki67 immunohistochemistry staining of tumors retrieved from treated mice in different groups with (+) and without (–) NIR irradiation.

reached 48 °C it was maintained constant for 5 min. The enhanced permeability and retention (EPR) effect of tumor cells could prolong the presence of the released photothermal agent at the inserted tumor site,[81] which is best for multiple PTT of the tumor followed by one MN insertion. So, on the fourth day of treatment, PTT (with no MN insertion) was induced in the +NIR groups. The tumor volume and body weight were also recorded every 2 days over 16 days without further treatment (Fig. 9a and b). In the control group (±NIR) the tumor volume rapidly grew and was 520% of the initial volume at day 4. As the control group, the PVP group with or without NIR and the PVP-Bi_2S_3 group without NIR irradiation exhibited similar results. Single administration of chemo or PTT agents in PVP-Bi_2S_3-SFN (−NIR) and PVP-Bi_2S_3 (+NIR) groups could slow the growth of tumor volume to 150% of the initial volume at day 4 which suggested limited inhibition efficiency of SFN and Bi_2S_3 NPs individually. The synergistic combination of the photothermal and chemotherapy factors showed a noteworthy inhibition effect on the tumor growth and obviously, the presented tumor was disrupted at day 2 of treatment. As mentioned above, PTT could promote the permeability of blood vessels and in this way, help the extra entrance of the drug molecules into melanoma cells, which persuades a more effective cancer treatment response than monotherapy. The monitoring of the mice's body weight further confirmed the biosafety of the treatment and no weight loss was observed during the examination (Fig. 9c). According to the survival rate of mice during 30 days, 50% of animals in the control group (±NIR) died on day 10 after treatment (Fig. 9d). This count was approximately 40% in the PVP (±NIR), 30% in PVP-Bi_2S_3 with no laser irradiation group, 16% in PVP-Bi_2S_3 with NIR irradiation, and no death occurred in the chemotherapy and combination therapy groups at day 10. Notably, a 100% survival rate 25 days after treatment was detected in PVP-Bi_2S_3-SFN with the NIR irradiation group and more than 65% over 30 days. However, in the monotherapy groups, all the mice died after 21 days but in the other groups, it was on day 16. To further evaluate therapeutic efficiency, the tumor tissue was analyzed with H&E-stained histopathology, and tumor cell proliferation was monitored using antigen Ki-67 staining. As shown in the H&E staining in Fig. 9e, the cancer cells of the PVP-Bi_2S_3 (+NIR) and PVP-Bi_2S_3-SFN (−NIR) groups treated through monotherapy exhibited preferable results compared with the control group, with low cell density, tumor necrosis, and nuclear impair. As expected, the PVP-Bi_2S_3-SFN (+NIR) group induced the most severe damage and extraordinary cell necrosis compared to other groups. The control and the blank groups (PVP (±NIR), PVP-Bi_2S_3 (−NIR)) exhibited a high density of blood vessels and no nuclear loss. Concurring with H&E staining information, high-rate cell growth was discovered at the control, PVP (±NIR), and PVP-Bi_2S_3 without NIR irradiation groups through Ki-67 staining. The anti-tumor activity of Bi_2S_3 NPs and SFN in the single therapy groups decreased the Ki-67 expression. However, the B16F10 cell proliferation and the rate of Ki-67 expression were very low under the synergistic effect of photothermal and chemotherapy in the PVP-Bi_2S_3-SFN (+NIR) group. The findings approved the outstanding intratumorally drug delivery and release potential of the proposed MN patches. Outside of the photothermal ability of synthesized NPs to suppress cancer cells under NIR exposure and the successful chemotherapy effect of released SFN, combined photothermal and chemotherapy promoted a synergistic effect and more powerfully inhibited tumor growth in mice. It is noteworthy that the cancer in the PVP-Bi_2S_3-SFN (+NIR) group recurred in some animals after 20 days of treatment which suggested an insufficient treatment regimen. To address this issue, it seems the MN insertion to administer combination therapy had to be done more than twice, was carried out in this study, and in different time intervals. Likewise, multiple studies demonstrated the combination of photothermal-immunotherapy,[82,83] photothermal-photodynamic-immunotherapy,[84] and photothermal-chemo-immunotherapy[85] could inhibit tumor recurrence. Therefore, the MN-mediated PTT in the presented study can accompany other methods to induce combination cancer therapy and prevent the cancer cells' recurrence effect. Despite the success of the drug delivery potential of the introduced MN-patch, it is recommended for the relatively short duration of the needle dissolution and insertion process, other high-potential dissolving polymers such as carboxymethyl cellulose (CMC), hyaluronic acid (HA), polyvinyl alcohol (PVA), poly(lactic acid-*co*-glycolic acid) (PLGA), gelatin, and copolymers like poly (methylvinylether/maleic anhydride) (PMVE-MA) can be studied to fabricate dissolvable MN-mediated drug delivery. In a study, the researchers demonstrated the HA-MN and PMVE-MA-MN patches could dissolve completely within 60 s after the porcine skin insertion.[86] Surely, a beneficial tumor drug delivery system must be further investigated and characterized besides dissolving ability, as assessed in this study on the PVP-based MN arrays. Furthermore, the confirmed local drug delivery potential of the MN patches to the desired site, made a significant result in a dose reduction required of SFN to inhibit tumor growth. According to FDA reports and studies, the recommended SFN dose for cancer treatment is 400 mg twice daily or 30 mg kg^{-1} orally,[87] or i.p. injection of 60 mg kg^{-1},[88] which is significantly higher than the SFN-loaded amount (19 ± 1 μg) in the present study. This underscores the strength of the resultant MN arrays in delivering drugs directly to the tumor site, without the risk of toxicity and side effects associated with conventional chemotherapy. The implications of this breakthrough are profound and bring us closer to a safe and effective cancer treatment.

4. Conclusions

An intertumoral drug delivery method was well established by fabricating the polymeric MN patch. The multiple-step solvent casting method was performed to prepare the tip-loaded MN arrays. In summary, the fabrication was victorious and the designed system revealed tolerable mechanical properties for skin insertion. The arrangement needles could pierce the under-study skin effectively and release the cargo into the skin after dissolving at an acceptable time. Additionally, the penetration depth study indicated the proposed patch had enough ability to deliver drugs into the skin's deeper layers in a time-dependent manner. Moreover, the synthesized Bi_2S_3 NPs with

approximately 40 nm in size showed high photothermal conversion efficiency *in vitro* and *in vivo* and so, could increase the temperature to an adequate degree for competent photothermal cancer therapy. In this study, SFN as a chemotherapy drug beside Bi_2S_3 NPs was successfully loaded into the PVP-based MN patch, resulting in no undesirable reaction that alleviated their therapeutic efficiency. The MN arrays with different formulations were blood and biocompatible with no toxicity effect on the main organs. Local drug delivery with the proposed patch and low SFN-loaded amount could prevent and manage the biodistribution and side effects of drugs on unneeded and healthy tissues which was confirmed through biosafety results. As compared to the single therapies, the combination of photothermal-chemotherapy on melanoma-induced BALB/c mice with the PVP-Bi_2S_3-SFN MN and NIR laser irradiation had a stunning growth inhibition effect on the B16F10 cells after 2 days of treatment which approves our claim of cancer combination therapy ability and promising drug delivery of the resultant dissolvable MN patch.

Conflicts of interest

There are no conflicts to declare.

Data availability

The data analysis of this article is available in the interactive notebook of Mahsa Akbari and can be provided by the authors upon request.

References

1 A. Fateeva, K. Eddy and S. Chen, *Cancers*, 2024, **16**, 1571.
2 M. H. Trager, L. J. Geskin, F. H. Samie and L. Liu, *Exp. Dermatol.*, 2022, **31**, 4–12.
3 J. Lopes, C. M. Rodrigues, M. M. Gaspar and C. P. Reis, *Cancers*, 2022, **14**, 4652.
4 G. Song, Y. Sun, T. Liu, X. Zhang, Z. Zeng, R. Wang, P. Li, C. Li and G. Jiang, *Chem. Eng. J.*, 2021, **426**, 130790.
5 L. Haas, A. Elewaut, C. L. Gerard, C. Umkehrer, L. Leiendecker, M. Pedersen, I. Krecioch, D. Hoffmann, M. Novatchkova and M. Kuttke, *Nat. Cancer*, 2021, **2**, 693–708.
6 S. Pizzimenti, S. Ribero, M. A. Cucci, M. Grattarola, C. Monge, C. Dianzani, G. Barrera and G. Muzio, *Antioxidants*, 2021, **10**, 1942.
7 A. M. Czarnecka, E. Bartnik, M. Fiedorowicz and P. Rutkowski, *Int. J. Mol. Sci.*, 2020, **21**, 4576.
8 A. Hendrickx, A. Cozzio, L. Plasswilm and C. M. Panje, *Radiat. Oncol.*, 2020, **15**, 1–8.
9 J. P. Pham, A. M. Joshua, I. P. da Silva, R. Dummer and S. M. Goldinger, *Curr. Oncol. Rep.*, 2023, **25**, 609–621.
10 L. Zeng, B. J. Gowda, M. G. Ahmed, M. A. Abourehab, Z.-S. Chen, C. Zhang, J. Li and P. Kesharwani, *Mol. Cancer*, 2023, **22**, 10.
11 L. Tagliaferri, V. Lancellotta, B. Fionda, M. Mangoni, C. Casà, A. Di Stefani, M. M. Pagliara, A. D'Aviero, G. Schinzari and S. Chiesa, *Hum. Vaccines Immunother.*, 2022, **18**, 1903827.
12 J. Jiang, X. Che, Y. Qian, L. Wang, Y. Zhang and Z. Wang, *Front. Mater.*, 2020, **7**, 234.
13 J. Hwang and J.-O. Jin, *Biomolecules*, 2020, **10**, 1124.
14 H. S. Han and K. Y. Choi, *Biomedicines*, 2021, **9**, 305.
15 M. IJff, J. Crezee, A. L. Oei, L. J. Stalpers and H. Westerveld, *Int. J. Gynecol. Cancer*, 2022, **32**, 288–296.
16 T. Chen, D. Cen, Z. Ren, Y. Wang, X. Cai, J. Huang, L. Di Silvio, X. Li and G. Han, *Biomaterials*, 2019, **221**, 119419.
17 H. Wang, J. Yang, P. Cao, N. Guo, Y. Li, Y. Zhao, S. Zhou, R. Ouyang and Y. Miao, *Chin. Chem. Lett.*, 2020, **31**, 3015–3026.
18 M.-A. Shahbazi, L. Faghfouri, M. P. Ferreira, P. Figueiredo, H. Maleki, F. Sefat, J. Hirvonen and H. A. Santos, *Chem. Soc. Rev.*, 2020, **49**, 1253–1321.
19 H. Zhou, H. Pan, F. Raza, H. Zafar, Y. Ge, N. Wang, R. Zheng, D. Zhang and Y. Yang, *Mater. Adv.*, 2024, **5**, 2456–2469.
20 Y. Huang, H. Lai, J. Jiang, X. Xu, Z. Zeng, L. Ren, Q. Liu, M. Chen, T. Zhang and X. Ding, *Asian J. Pharm. Sci.*, 2022, **17**, 679–696.
21 Y. Liu, G. Zhang, Q. Li, J. Chen, W. Luo, X. Li, X. Suo, S. Li, Y. Xu and T. Liu, *Chem. Eng. J.*, 2024, 151437.
22 O. O. Peltek, T. E. Karpov, A. Rogova, A. Postovalova, E. Ageev, A. Petrov, D. Antuganov, A. A. Stanzhevsky, D. N. Maistrenko and D. Zuev, *ACS Appl. Mater. Interfaces*, 2023, **15**, 13460–13471.
23 M. Hasannia, K. Abnous, S. M. Taghdisi, A. Sazgarnia, S. Nekooei, M. Ramezani and M. Alibolandi, *J. Drug Delivery Sci. Technol.*, 2024, **94**, 105526.
24 R. Zhang, Q. Miao, D. Deng, J. Wu, Y. Miao and Y. Li, *Colloids Surf., B*, 2023, **226**, 113302.
25 R. F. Donnelly and M. R. Prausnitz, *Drug Delivery Transl. Res.*, 2024, **14**, 573–580.
26 M. Kirkby, A. R. J. Hutton and R. F. Donnelly, *Pharm. Res.*, 2020, **37**, 117.
27 M. Li, L. Yang, C. Wang, M. Cui, Z. Wen, Z. Liao, Z. Han, Y. Zhao, B. Lang, H. Chen, J. Qian, Y. Shu, X. Zeng and C. Sun, *ACS Nano*, 2023, **17**, 24200–24217.
28 S.-S. Moon, M. Richter-Roche, T. K. Resch, Y. Wang, K. R. Foytich, H. Wang, B. A. Mainou, W. Pewin, J. Lee, S. Henry, D. V. McAllister and B. Jiang, *npj Vaccines*, 2022, **7**, 26.
29 L. Junqueira, H. Polonini, C. Ramos, A. O. Ferreira, N. Raposo and M. Brandão, *Curr. Drug Delivery*, 2022, **19**, 614–624.
30 R. Parhi, *J. Drug Delivery Sci. Technol.*, 2022, **75**, 103639.
31 S. Li, D. Xia and M. R. Prausnitz, *Adv. Funct. Mater.*, 2021, **31**, 2103359.
32 A. F. Moreira, C. F. Rodrigues, T. A. Jacinto, S. P. Miguel, E. C. Costa and I. J. Correia, *Int. J. Pharm.*, 2020, **576**, 118907.
33 S. Lin, H. Lin, M. Yang, M. Ge, Y. Chen and Y. Zhu, *Nanoscale*, 2020, **12**, 10265–10276.

34 S. Abbaszadeh, M. R. Eskandari, V. Nosrati-Siahmazgi, K. Musaie, S. Mehrabi, R. Tang, M. R. Jafari, B. Xiao, V. Hosseinpour Sarmadi, F. Haghi, B. Z. Chen, X. D. Guo, H. A. Santos and M.-A. Shahbazi, *Mater. Today Bio*, 2023, **19**, 100609.
35 T. Takeda, M. Tsubaki, N. Kato, S. Genno, E. Ichimura, A. Enomoto, M. Imano, T. Satou and S. Nishida, *Oncol. Lett.*, 2021, **22**, 827.
36 J. Wawszczyk, R. Wolan, S. Smolik and M. Kapral, *Saudi Pharm. J.*, 2023, **31**, 1306–1316.
37 J. Arumugam, A. D. Raj and A. A. Irudayaraj, *Mater. Today: Proc.*, 2018, **5**, 16094–16099.
38 Z. Q. Zhao, B. Z. Chen, J. L. Gan, Y. H. Feng, L. Liang, L. Yu, Z. Y. Wang, S. Abbaszadeh, M.-A. Shahbazi and R. Yu, *Nano Res.*, 2024, 1–13.
39 J. Y. Lee, S. H. Dong, K. W. Ng and C. F. Goh, *Drug Delivery Transl. Res.*, 2025, 1–18.
40 G. C. Carvalho, M. N. V. Domingues, G. D. Marena, E. Mäkilä, J. Li, G. Geertsema-Doornbusch, C. R. de Andrade, M. C. Stuart, M. A. Shahbazi and I. Corrêa, *Adv. Ther.*, 2025, **8**, 2400342.
41 Z. Fatfat, M. Karam, B. Maatouk, D. Fahs and H. Gali-Muhtasib, *Advanced and Modern Approaches for Drug Delivery*, 2023, pp. 159–197.
42 E. Joseph and G. Singhvi, in *Nanomaterials for Drug Delivery and Therapy*, ed. A. M. Grumezescu, William Andrew Publishing, 2019, pp. 91–116, DOI: 10.1016/B978-0-12-816505-8.00007-2.
43 G. Horvat, M. Pantić, Ž. Knez and Z. Novak, *Gels*, 2022, **8**, 438.
44 Y.-C. Hung, S.-C. Hsieh, S.-R. Hou, J.-Y. Kung, C.-M. Tang and C.-J. Chang, *Appl. Sci.*, 2021, **11**, 10290.
45 S.-W. Huang, Y.-F. Lin, Y.-X. Li, C.-C. Hu and T.-C. Chiu, *Molecules*, 2019, **24**, 1785.
46 M. Chen, H. Qu, J. Zhu, Z. Luo, A. Khasanov, A. S. Kucknoor, N. Haldolaarachchige, D. P. Young, S. Wei and Z. Guo, *Polymer*, 2012, **53**, 4501–4511.
47 I. Uddin, S. M. Abzal, K. Kalyan, S. Janga, A. Rath, R. Patel, D. K. Gupta, T. Ravindran, H. Ateeq and M. S. Khan, *ACS Omega*, 2022, **7**, 42438–42445.
48 M. M. Elsayed, M. E. Mostafa, E. Alaaeldin, H. A. Sarhan, M. S. Shaykoon, S. Allam, A. R. Ahmed and B. E. Elsadek, *Int. J. Nanomed.*, 2019, 8445–8467.
49 I. Galain, M. Cardoso, E. Tejería, G. Mourglia-Ettlin, P. Arbildi, M. Terán, M. Pérez Barthaburu and I. Aguiar, *J. Nanopart. Res.*, 2022, **24**, 68.
50 K. Kavi Rasu, D. Vishnushankar and V. Veeravazhuthi, *Adv. Mater. Res.*, 2013, **678**, 248–252.
51 S. Khataei, M. H. Al-Musawi, K. Asadi, S. Ramezani, M. Abbasian and M. Ghorbani, *J. Drug Delivery Sci. Technol.*, 2023, **82**, 104310.
52 I. M. Alibe, K. A. Matori, M. H. M. Zaid, S. Nasir, A. M. Alibe and M. Z. A. Khiri, *Materials*, 2021, **14**, 1118.
53 U. Ruman, K. Buskaran, G. Pastorin, M. J. Masarudin, S. Fakurazi and M. Z. Hussein, *Nanomaterials*, 2021, **11**, 497.
54 M. Algethami, M. Geso, T. Piva, A. Blencowe, L. Lu, K. Ai, P. Harty and E. Gan, *NanoWorld J.*, 2015, **1**, 99–104.
55 H. Lu, X. Jin, S. Tong, M. Jin, Z. Zhu, J. Fang, G. Zhong, J. Chen, M. Deng and F. Chen, *Chem. Eng. Technol.*, 2023, **46**, 2233–2238.
56 N. H. Abdullah, Z. Zainal, S. Silong, M. I. M. Tahir, K.-B. Tan and S.-K. Chang, *Thermochim. Acta*, 2016, **632**, 37–45.
57 T. O. Ajiboye and D. C. Onwudiwe, *Results Chem.*, 2021, **3**, 100151.
58 H. Zhang, G. Chen, B. Yu, Y. Shen and H. Cong, *ACS Appl. Bio Mater.*, 2019, **2**, 3870–3876.
59 Q. Hao, Y. Huang, D. Chen, Y. Liu, W. Wei and B.-J. Ni, *Chin. J. Catal.*, 2020, **41**, 249–258.
60 Z. Guo, S. Zhu, Y. Yong, X. Zhang, X. Dong, J. Du, J. Xie, Q. Wang, Z. Gu and Y. Zhao, *Adv. Mater.*, 2017, **29**, 1704136.
61 Y. Lu, L. Li, Z. Lin, M. Li, X. Hu, Y. Zhang, M. Peng, H. Xia and G. Han, *Adv. Healthcare Mater.*, 2018, **7**, 1800602.
62 A. C. Doughty, A. R. Hoover, E. Layton, C. K. Murray, E. W. Howard and W. R. Chen, *Materials*, 2019, **12**, 779.
63 A. V. P. Kumar, S. K. Dubey, S. Tiwari, A. Puri, S. Hejmady, B. Gorain and P. Kesharwani, *Int. J. Pharm.*, 2021, **606**, 120848.
64 R. Zhou, Q. Zhou, G. Ling and P. Zhang, *Colloids Surf., A*, 2023, **660**, 130832.
65 S. Yadav and P. K. Maurya, *3 Biotech*, 2022, **12**, 28.
66 A. Tkachenko, *Toxicol. In Vitro*, 2024, 105814.
67 H. T. T. Duong, Y. Yin, T. Thambi, B. S. Kim, J. H. Jeong and D. S. Lee, *J. Mater. Chem. B*, 2020, **8**, 1171–1181.
68 A. Hou, G. Quan, B. Yang, C. Lu, M. Chen, D. Yang, L. Wang, H. Liu, X. Pan and C. Wu, *Adv. Healthcare Mater.*, 2019, **8**, 1900898.
69 X. Zhao, X. Li, P. Zhang, J. Du and Y. Wang, *J. Controlled Release*, 2018, **286**, 201–209.
70 X. Xiu, G. Gao, Y. Liu and F. Ma, *J. Drug Delivery Sci. Technol.*, 2022, **76**, 103653.
71 D. Ando, M. Miyatsuji, H. Sakoda, E. Yamamoto, T. Miyazaki, T. Koide, Y. Sato and K.-I. Izutsu, *Pharmaceutics*, 2024, **16**, 200.
72 P. Makvandi, M. Kirkby, A. R. Hutton, M. Shabani, C. K. Yiu, Z. Baghbantaraghdari, R. Jamaledin, M. Carlotti, B. Mazzolai and V. Mattoli, *Nano-Micro Lett.*, 2021, **13**, 1–41.
73 S. A. Ranamukhaarachchi and B. Stoeber, *Biomed. Microdevices*, 2019, **21**, 1–8.
74 M.-H. Lee, H. Seo, M.-S. Lee, B. J. Kim, H. L. Kim, D. H. Lee, J. Oh, J. Y. Shin, J. Y. Jin and D. H. Jeong, *Front. Immunol.*, 2023, **14**, 1178688.
75 A. J. Paredes, F. Volpe-Zanutto, L. K. Vora, I. A. Tekko, A. D. Permana, C. J. Picco, H. O. McCarthy and R. F. Donnelly, *Mater. Today Bio*, 2022, **13**, 100217.
76 G. Maguire, *J. Tissue Viability*, 2022, **31**, 687–692.
77 İ. İ. Öztürk and M. G. ESER, *Hittite J. Sci. Eng.*, 2022, **9**, 225–233.
78 Y. Qiao, X. Jia, Y. Wang, L. Liu, M. Zhang and X. Jiang, *Nanoscale Horiz.*, 2024, **9**, 1002–1012.
79 N. Xu, X. Zhang, T. Qi, Y. Wu, X. Xie, F. Chen, D. Shao and J. Liao, *MedComm: Biomater. Appl.*, 2022, **1**, e25.

80 P. Wang, B. Chen, Y. Zhan, L. Wang, J. Luo, J. Xu, L. Zhan, Z. Li, Y. Liu and J. Wei, *Pharmaceutics*, 2022, **14**, 2279.
81 H. Tian, T. Zhang, S. Qin, Z. Huang, L. Zhou, J. Shi, E. C. Nice, N. Xie, C. Huang and Z. Shen, *J. Hematol. Oncol.*, 2022, **15**, 132.
82 W. Li, T. Ma, T. He, Y. Li and S. Yin, *Chem. Eng. J.*, 2023, **463**, 142495.
83 W. Chen, Z. Guo, Y. Zhu, N. Qiao, Z. Zhang and X. Sun, *Adv. Funct. Mater.*, 2020, **30**, 1906623.
84 R. Lima-Sousa, B. L. Melo, C. G. Alves, A. F. Moreira, A. G. Mendonça, I. J. Correia and D. de Melo-Diogo, *Adv. Funct. Mater.*, 2021, **31**, 2010777.
85 A. Wang, X. Yang, R. Li, L. Shao, W. Zhao, X. Hu, K. Fang, K. Chai, S. Shi and C. Dong, *ACS Appl. Mater. Interfaces*, 2023, **15**, 53318–53332.
86 M. C. Lobita, N. El-Sayed, J. F. Pinto and H. A. Santos, *Int. J. Pharm.*, 2023, **642**, 123143.
87 M. Gerwing, E. Hoffmann, C. Geyer, A. Helfen, B. Maus, R. Schinner, L. Wachsmuth, W. Heindel, M. Eisenblaetter, C. Faber and M. Wildgruber, *Transl. Oncol.*, 2023, **37**, 101773.
88 S. A. Wohlfeil, V. Häfele, B. Dietsch, C. Weller, C. Sticht, A. S. Jauch, M. Winkler, C. D. Schmid, A. L. Irkens and A. Olsavszky, *J. Transl. Med.*, 2022, **20**, 62.